REMOTE SENSING BY RADAR

Radar remote sensing instruments acquire data useful for geophysical investigations by measuring electromagnetic interactions with natural objects. Examples of radar remote sensing instruments include synthetic aperture radars (SARs), scatterometers, altimeters, radar sounders, and meteorological radars such as cloud and rain radars. The main advantage of radar instruments is their ability to penetrate clouds, rain, tree canopies, and even dry soil surfaces depending upon the operating frequencies. In addition, since a remote sensing radar is an active instrument, it can operate day and night by providing its own illumination.

Imaging remote sensing radars such as SAR produce high-resolution (from submeter to a few tens of meters) images of surfaces. The geophysical information can be derived from these high-resolution images by using proper postprocessing techniques. Scatterometers measure the backscattering cross section accurately in order to characterize surface properties such as roughness. Altimeters are used to obtain accurate surface height maps by measuring the round-trip time delay from a radar sensor to the surface. Radar sounders can image underground material variations by penetrating deeply into the ground. Unlike surveillance radars, remote sensing radars require accurate calibration in order for the data to be useful for scientific applications.

In this article, we start with the basic principles of remote sensing radars. Then, we discuss the details of imaging radars and their applications. In order to complete the remote sensing radar discussion, we briefly examine nonimaging radars such as scatterometers, altimeters, radar sounders, and meteorological radars. For more information on these types of radars, the interested reader is referred to other articles in this encyclopedia. We also provide extensive references for each radar for readers who need an in-depth description of a particular radar.

RADAR PRINCIPLES

We start our discussion with the principles necessary to understand the radar remote sensing instruments that will be described in the later part of this article. For more detailed discussions, readers are referred to Refs. 1–3.

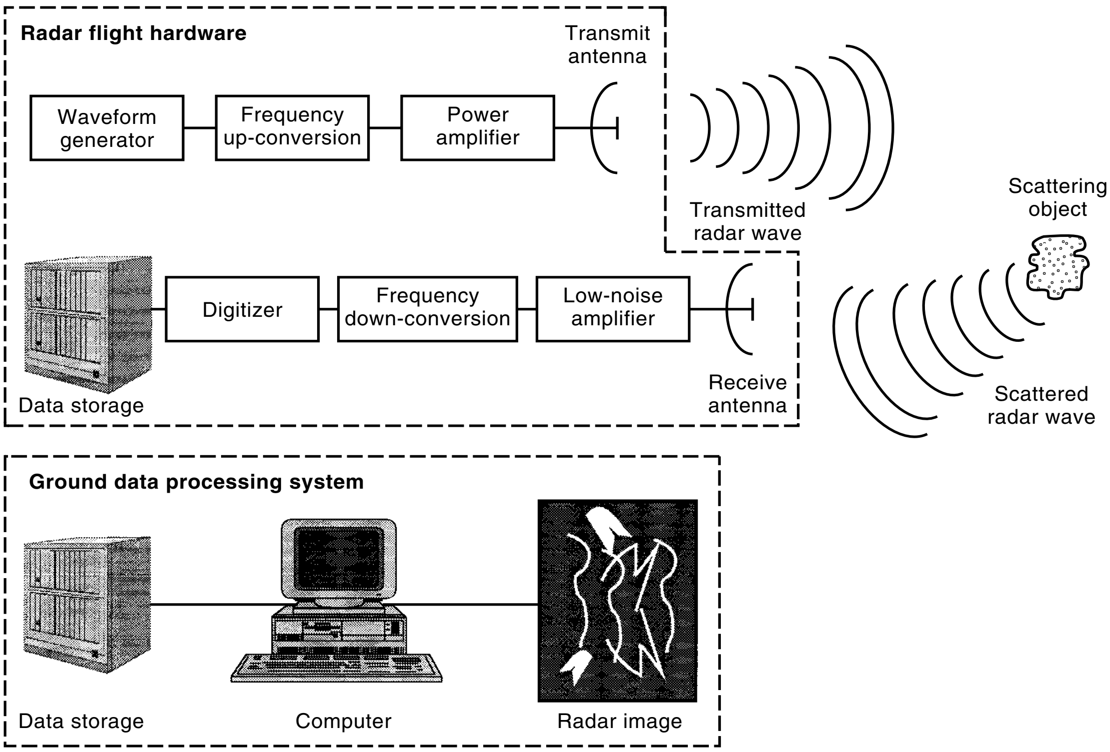

Figure 1. The basic components of a radar system. A pulse of energy is transmitted from the radar system antenna, and after a time delay an echo is received and recorded. The recorded radar echoes are later processed into images. The flight electronics are carried on the radar platform, either an aircraft or a spacecraft. Image processing is usually done in a ground facility.

Radar Operation

A radar transmits an electromagnetic signal and receives and records the echo reflected from the illuminated terrain. Hence, a radar is an active remote sensing instrument since it provides its own illumination. The basic radar operation is illustrated by Fig. 1. A desired signal waveform, commonly a modulated pulse, is generated by a waveform generator. After proper frequency upconversion and high-power amplification, the radar signal is transmitted from an antenna. The reflected echo is received by the antenna, and it is amplified and down-converted to video frequencies for digitization. The digitized data are either stored in a data recorder for later ground data processing or processed by an on-board data processor. Since remote sensing radars usually image large areas, they are commonly operated from either an airborne or a spaceborne platform.

Basic Principles of Radar Imaging

Imaging radars generate surface images very similar to visible and infrared images. However, the principle behind the image generation is fundamentally different in the two cases. Visible and infrared sensors use a lens or mirror system to project the radiation from the scene on a "two-dimensional array of detectors" which could be an electronic array or a film using chemical processes. The two-dimensionality can also be achieved by using scanning systems. This imaging approach conserves the angular relationships between two targets and their images as shown in Fig. 2.

Imaging radars use the time delay between the echoes that are backscattered from different surface elements to separate them in the *range* (cross-track) dimension, and they use the angular size (in the case of the real-aperture radar) or the Doppler history (in the case of the synthetic-aperture radar) to separate surface pixels in the *azimuth* (along-track) dimension. The imaging radar sensor uses an antenna which illuminates the surface to one side of the flight track. Usually, the antenna has a fan beam which illuminates a highly elongated

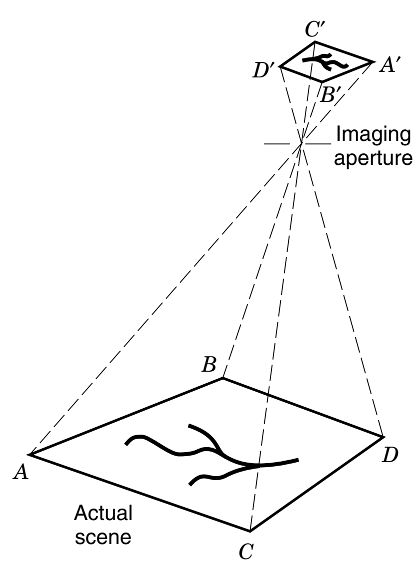

Figure 2. Optical imaging systems preserve the angular relationship between objects in the image.

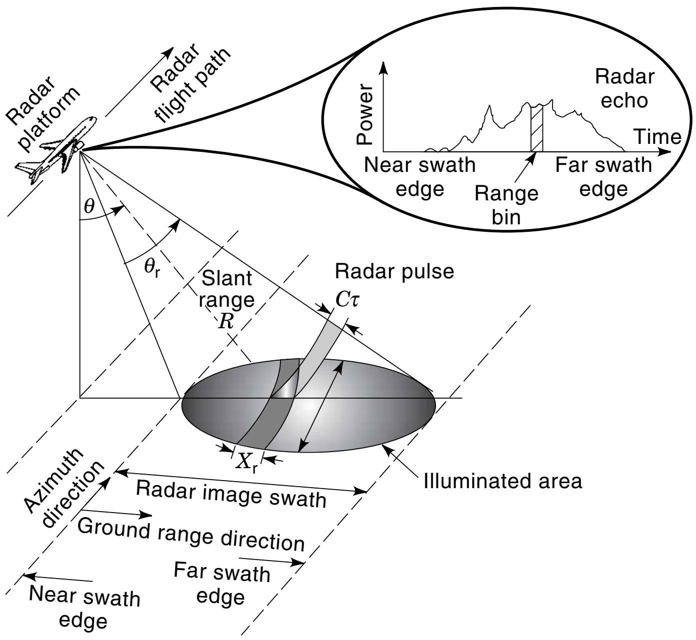

Figure 3. Radar imaging geometry and definition of terms.

elliptical-shaped area on the surface as shown in Fig. 3. The illuminated area across track defines the image *swath.* Within the illumination beam, the radar sensor transmits a very short effective pulse of electromagnetic energy. Echoes from surface points farther away along the cross-track coordinate will be received at proportionally later time (Fig. 3). Thus, by dividing the receive time in increments of equal time bins, the surface can be subdivided into a series of *range bins.* The width in the along-track direction of each range bin is equal to the antenna footprint along the track, x_a. As the platform moves, the sets of range bins are covered sequentially, thus allowing strip mapping of the surface line by line. This is comparable to strip mapping with a pushbroom imaging system using a line array in the visible and infrared part of the electromagnetic spectrum. The brightness associated with each image pixel in the radar image is proportional to the echo power contained within the corresponding time bin. As we will see later, the different types of imaging radars really differ in the way in which the azimuth resolution is achieved.

The *look angle* is defined as the angle between the vertical direction and the radar beam at the radar platform, while the *incidence angle* is defined as the angle between the vertical direction and the illuminating radar beam at the surface. When surface curvature effects are neglected, the look angle is equal to the incidence angle at the surface when the surface is flat. In the case of spaceborne systems, surface curvature must be taken into account, which leads to an incidence angle that is always larger than the look angle (3) for flat surfaces. If topography is present (i.e., the surface is not flat), the local incidence angle may vary from radar image pixel to pixel.

Resolution

The resolution is defined as the surface separation between the two closest features that can still be resolved in the final image. First, consider two point targets that are separated in the range direction by x_r. The corresponding echoes will be separated by a time difference Δt equal to

$$\Delta t = \frac{2x_r \sin\theta}{c} \tag{1}$$

where c is the speed of light and the factor 2 is included to account for the signal round-trip propagation. The angle θ in Eq. (1) is the incidence angle. The two features can be discriminated if the leading edge of the pulse returned from the second object is received later than the trailing edge of the pulse received from the first feature. Therefore, the smallest discriminable time difference in the radar receiver is equal to the pulse effective time length τ. Thus,

$$\frac{2x_r \sin\theta}{c} = \tau \Rightarrow x_r = \frac{c\tau}{2\sin\theta} \tag{2}$$

In other words, the range resolution is equal to half the footprint of the radar pulse on the surface. Sometimes the effective pulse length is described in terms of the system bandwidth B. To a good approximation, we have

$$\tau = \frac{1}{B} \tag{3}$$

The sin θ term in the denominator of Eq. (2) means that the ground range resolution of an imaging radar will be a strong function of the look angle at which the radar is operated. To illustrate, a signal with a bandwidth B = 20 MHz (i.e., effective pulse length τ = 50 ns) provides a range resolution of 22 m for $\theta = 20°$, while a signal bandwidth B = 50 MHz (τ = ns) provides a range resolution of 4.3 m at $\theta = 45°$.

In the azimuth direction, without further data processing, the resolution x_a is equal to the beam footprint on the surface that is defined by the azimuth beamwidth of the radar antenna θ_a given by

$$\theta_a = \frac{\lambda}{L} \tag{4}$$

from which it follows that

$$x_a = \frac{h\theta_a}{\cos\theta} = \frac{\lambda h}{L\cos\theta} \tag{5}$$

where L is the azimuth antenna length, and h is the altitude of the radar above the surface being imaged. To illustrate, for h = 800 km, λ = 23 cm, L = 12 m, and $\theta = 20°$ we obtain x_a = 16 km. Even if λ is as short as 2 cm and h is as low as 200 km, x_a will still be equal to about 360 m, which is considered to be a relatively low resolution, even for remote sensing. This has led to very limited use of the real-aperture technique for surface imaging, especially from space. Equation (5) is also directly applicable to optical imagers. However, because of the small value of λ (about 1 μm), resolutions of a few meters can be achieved from orbital altitudes with an aperture only a few tens of centimeters in size.

When the radar antenna travels along the line of flight, two point targets at the different angles from the flight track have different Doppler frequency. Using this Doppler frequency spread, one can obtain a higher resolution in the along track direction. As shown in the synthetic aperture radar section, the along-track resolution can be as small as the half of the antenna length in the along-track direction. This method is often called the Doppler beam sharpening.

Radar Equation

One of the key factors that determine the quality of the radar imagery is the corresponding *signal-to-noise* ratio (SNR). This is the equivalent of the brightness of a scene being photographed with a camera versus the sensitivity of the film or detector. Here, we consider the effect of thermal noise on the sensitivity of radar imaging systems.

Let P_t be the sensor-generated peak power transmitted out of the antenna. One function of the antenna is to focus the radiated energy into a small solid angle directed toward the area being imaged. This focusing effect is described by the antenna gain G, which is equal to the ratio of the total solid angle over the solid angle formed by the antenna beam:

$$G = \frac{4\pi}{\theta_r\theta_a} = \frac{4\pi LW}{\lambda^2} = \frac{4\pi A}{\lambda^2} \tag{6}$$

where L is the antenna length in the flight track direction, W is the antenna length in the cross track direction, and A is the antenna area. The radiated wave propagates spherically away from the antenna toward the surface. Thus the power density P_i per unit area incident on the illuminated surface is

$$P_i = \frac{P_t G}{4\pi R^2} \tag{7}$$

The backscattered power P_s from an illuminated surface area s is given by

$$P_s = P_i s \sigma_0 \tag{8}$$

where σ_0 is the surface normalized *backscattering cross section* which represents the efficiency of the surface in re-emitting back toward the sensor some of the energy incident on it. It is similar to the surface albedo at visible wavelengths. The backscattered energy propagates spherically back toward the sensor. The power density P_c at the antenna is then

$$P_c = \frac{P_s}{4\pi R^2} \tag{9}$$

and the total received power is equal to the power intercepted by the antenna:

$$P_r = P_c A \tag{10}$$

or

$$P_r = \frac{P_t G_t}{4\pi R^2} s\sigma_0 \frac{\lambda^2 G_r}{(4\pi R)^2} \tag{11}$$

In Eq. (11) we explicitly show that the transmit and receive antennas may have different gains. This is important for the more advanced SAR techniques like polarimetry where antennas with different polarizations may be used during transmission and reception.

In addition to the target echo, the received signal also contains noise which results from the fact that all objects at temperatures higher than absolute zero emit radiation across the whole electromagnetic spectrum. The noise component that is within the spectral bandwidth B of the sensor is passed through with the signal. The thermal noise power is given by

$$P_N = kTB \tag{12}$$

where k is Boltzmann's constant ($k = 1.38 \times 10^{-23}$ J/K) and T is the total equivalent noise temperature. The resulting SNR is then

$$\text{SNR} = P_r/P_N \tag{13}$$

One common way of characterizing an imaging radar sensor is to determine the surface backscatter cross section σ_N which gives an SNR = 1. This is called the *noise equivalent backscatter cross section.* It defines the weakest surface return that can be detected, and therefore the range of surface units that can be imaged.

Backscattering Cross Section and Calibration Devices

The *normalized backscattering cross section* represents the reflectivity of an illuminated area in the backscattering direction. A higher backscattering cross section means that the area more strongly reflects the incidence radar signal. It is mathematically defined as

$$\sigma_0 = \lim_{R,A_i\to\infty}\left\{\frac{4\pi R^2}{A_i}\frac{\langle E_s E_s^*\rangle}{E_i E_i^*}\right\} \tag{14}$$

where A_i is the illuminated area and E_s and E_i are the scattered and incident electric fields, respectively. In order to calibrate the radar data, active and/or passive calibration devices are commonly used.

By far the most commonly used passive calibration device is a trihedral corner reflector which consists of three triangular panels bolted together to form right angles with respect to each other. The maximum radar cross section (RCS) of a trihedral corner reflector is given by

$$\text{RCS} = \frac{4\pi a^4}{3\lambda^2} \tag{15}$$

where a is the long-side triangle length of a trihedral corner reflector. This reflector has about 40° half-power beamwidth which makes the corner reflector response relatively insensitive to the position errors. In addition, these devices are easily deployed in the field; and since they require no power to operate, they can be used unattended in remote locations under most weather conditions.

Signal Modulation

A pulsed radar determines the range by measuring the round-trip time by transmitting a pulse signal. In designing the signal pattern for a radar sensor, there is usually a strong requirement to have as much energy as possible in each pulse in order to enhance the SNR. This can be done by increasing the peak power or by using a longer pulse. However, particularly in the case of spaceborne sensors, the peak power is usually strongly limited by the available power devices. On the other hand, an increased pulse length (i.e., smaller bandwidth) leads to a worse range resolution [see Eq. (2)]. This dilemma is usually resolved by using *modulated* pulses which have the property of a wide bandwidth even when the pulse is very long. One such modulation scheme is the linear frequency modulation or chirp.

In a chirp, the signal frequency within the pulse is linearly changed as a function of time. If the frequency is linearly changed from f_0 to $f_0 + \Delta f$, the effective bandwidth would be equal to

$$B = |(f_0 + \Delta f) - f_0| = |\Delta f| \tag{16}$$

which is independent of the pulse length. Thus a pulse with long duration (i.e., high energy) and wide bandwidth (i.e., high range resolution) can be constructed. The instantaneous frequency for such a signal is given by

$$f(t) = f_0 + \frac{B}{\tau'} t \qquad \text{for } -\frac{\tau'}{2} \le t \le \frac{\tau'}{2} \tag{17}$$

and the corresponding signal amplitude is

$$A(t) \sim \cos[\textstyle\int f(t)\,dt] = \cos\left[f_0 t + \frac{B}{2\tau'} t^2\right] \tag{18}$$

Note that the instantaneous frequency is the derivative of the instantaneous phase. A pulse signal such as Eq. (18) has a physical pulse length τ' and a bandwidth B. The product $\tau' B$ is known as the *time bandwidth product* of the radar system. In typical radar systems, time bandwidth products of several hundred are used.

At first glance it may seem that using a pulse of the form Eq. (18) cannot be used to separate targets that are closer than the projected physical length of the pulse. It is indeed true that the echoes from two neighboring targets which are separated in the range direction by much less than the physical length of the signal pulse will overlap in time. If the modulated pulse, and therefore the echoes, have a constant frequency, it will not be possible to resolve the two targets. However, if the frequency is modulated as described in Eq. (18), the echoes from the two targets will have different frequencies at any instant of time and therefore can be separated by frequency filtering. In actual radar systems, a matched filter is used to *compress* the returns from the different targets. It can be shown (3) that the effective pulse length of the compressed pulse is given by Eq. (3). Therefore, the achievable range resolution using a modulated pulse of the kind given by Eq. (18) is a function of the chirp bandwidth, and not the physical pulse length. In typical spaceborne and airborne SAR systems, physical pulse lengths of several tens of microseconds are used, while bandwidths of several tens of megahertz are no longer uncommon for spaceborne systems, and several hundreds of megahertz are common in airborne systems.

REAL APERTURE RADAR

The real aperture imaging radar sensor uses an antenna which illuminates the surface to one side of the flight track. Usually, the antenna has a fan beam which illuminates a highly elongated elliptical shaped area on the surface as shown in Fig. 3. As mentioned before, the illuminated area across track defines the image swath. For an antenna of width W operating at a wavelength λ, the beam angular width in the range plane is given by

$$\theta_r \approx \frac{\lambda}{W} \tag{19}$$

and the resulting surface footprint or swath S is given by

$$S \approx \frac{h\theta_r}{\cos^2\theta} = \frac{\lambda h}{W\cos^2\theta} \tag{20}$$

where h is the sensor height above the surface, θ is the angle from the center of the illumination beam to the vertical (known as the *look angle* at the center of the swath), and θ_r is assumed to be very small. To illustrate, for λ = 27 cm, h = 800 km, θ = 20°, and W = 2.1 m, the resulting swath width is 100 km.

As shown before, the main disadvantage of the real aperture radar technique is the relatively poor azimuth resolution that could be achieved from space. From aircraft altitudes, however, reasonable azimuth resolutions can be achieved if higher frequencies (typically X-band or higher) are used. For this reason, real aperture radars are not commonly used any more.

SYNTHETIC APERTURE RADAR

Synthetic aperture radar refers to a particular implementation of an imaging radar system that utilizes the movement of the radar platform and specialized signal processing to generate high-resolution images. Prior to the discovery of the synthetic aperture radar principle, imaging radars operated using the real aperture principle and were known as side-looking airborne radars (SLARs).

Carl Wiley of the Goodyear Aircraft Corp. is generally credited as the first person to describe the use of Doppler frequency analysis of signals from a moving coherent radar to improve along-track resolution. He noted that two targets at different along-track positions will be at different angles relative to the aircraft velocity vector, resulting in different Doppler frequencies. Therefore, targets can be separated in the along-track direction on the basis of their different Doppler frequencies. This technique was originally known as Doppler beam sharpening, but later became known as synthetic aperture radar (SAR). The reader interested in a discussion of the history of SAR, both airborne and spaceborne, is referred to an excellent discussion in Chap. 1 of Ref. 3.

In this section we discuss the principles of radar imaging using synthetic-aperture techniques, the resulting image projections, distortions, tonal properties, and environmental effects on the images. We have attempted to give simple explanations of the different imaging radar concepts. For more detailed mathematical analysis the reader is referred to specialized texts such as Refs. 1–3.

Synthetic Aperture Radar Principle

As discussed in the previous section, a real-aperture radar cannot achieve high azimuth resolution from an orbital platform. In order to achieve a high resolution from any altitude, the synthetic-aperture technique is used. This technique uses successive radar echoes acquired at neighboring locations along the flight line to synthesize an equivalent very long antenna which provides a very narrow beamwidth and thus a high image resolution. In this section we explain SAR using two different approaches, namely, the synthetic array approach and the Doppler synthesis approach, which lead to the same results. We will also discuss uses of linear frequency modulation (chirp) as well as some limitations and degradation that are inherent to the SAR technique. Our discussion closely follows that of Ref. 1.

The range resolution and radar equation derived previously for a real aperture radar are still valid here. The main difference between real and synthetic aperture radars is in the way in which the azimuth resolution is achieved.

Synthetic Array Approach. The synthetic array approach explains the SAR technique by comparing it to a long array of antennas and the resulting increase in the resolution relative to the resolution achieved with one of the array elements. Let us consider a linear array of antennas consisting of N elements (Fig. 4). The contribution of the nth element to the total far field electric field E in the direction β is proportional to

$$E_{\mathrm{r}} \sim a_n e^{i\phi_n} e^{-ikd_n \sin\beta} \tag{21}$$

where a_n and ϕ_n are the amplitude and phase of the signal radiated from the nth element, d_n is the distance of the nth element to the array center, and $k = 2\pi/\lambda$. The total electric field is given by

$$E(\beta) \sim \sum_n a_n e^{i\phi_n} e^{-ikd_n \sin\beta} \tag{22}$$

If all the radiators are identical in amplitude and phase and are equally spaced with a separation d, then

$$E(\beta) \sim ae^{i\phi} \sum_n e^{-inkd\sin\beta} \tag{23}$$

This is the vector sum of N equal vectors separated by a phase $\Psi = kd \sin \beta$. The resulting vector shown in Eq. (23) has the following properties:

- For $\beta = 0 \Rightarrow \Psi = 0 \Rightarrow$, all vectors add together leading to a maximum for E.
- As β increases, the elementary vectors will spread and lead to a decrease in the magnitude of E.
- For β such that $N\Psi = 2\pi$, the vectors are spread all around a circle, leading to a sum equal to zero.

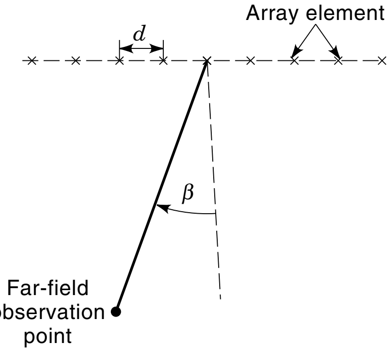

Figure 4. Geometry of a linear array of antenna elements.

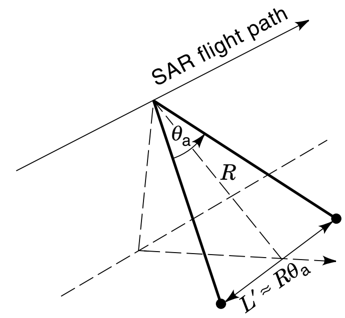

Figure 5. The width of the antenna beam in the azimuth direction defines the length of the synthetic aperture.

Thus, the radiation pattern has a null for

$$Nkd\sin\beta = 2\pi \Rightarrow \beta = \sin^{-1}\left(\frac{2\pi}{Nkd}\right) = \sin^{-1}\left(\frac{\lambda}{D}\right) \tag{24}$$

where $D = Nd$ is the total physical length of the array.

From the above it is seen that an array of total length $D = Nd$ has a beamwidth equal to the one for a continuous antenna of physical size D. This is achieved by adding the signals from each element in the array coherently—that is, amplitude and phase. The fine structure of the antenna pattern depends on the exact spacing of the array. Close spacing of the array elements is required to avoid grating effects.

In a conventional array, the signals from the different elements are combined together with a network of waveguides or cables leading to a single transmitter and receiver. Another approach is to connect each element to its own transmitter and receiver. The signals are coherently recorded and added later using a separate processor. A third approach could be used if the scene is quasi-static. A single transmitter/receiver/antenna element can be moved from one array position to the next. At each location a signal is transmitted and the echo recorded coherently. The echoes are then added in a separate processor or computer. A stable oscillator is used as a reference to ensure coherency as the single element moves along the array line. This last configuration is used in a SAR where a single antenna element serves to synthesize a large aperture.

Referring to Fig. 5, it is clear that if the antenna beam is equal to $\theta_{\mathrm{a}} = \lambda/L$, the maximum possible synthetic aperture length that would allow us to observe a point is given by

$$L' = R\theta_{\mathrm{a}} \tag{25}$$

This synthetic array will have a beamwidth θ_{s} equal to

$$\theta_{\mathrm{s}} = \lambda/2L' = \lambda/(2R\theta_{\mathrm{a}}) = L/(2R) \tag{26}$$

The factor 2 is included to account for the fact that the 3 dB (half-power) beamwidth is narrower in a radar configuration where the antenna pattern is involved twice, once each at transmission and reception. The corresponding surface along-track resolution of the synthetic array is

$$x_{\mathrm{a}} = R\theta_{\mathrm{s}} = \frac{L}{2} \tag{27}$$

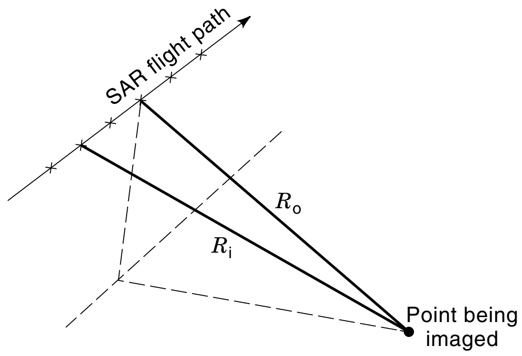

Figure 6. For large synthetic arrays, one has to compensate during ground processing for the change in geometry between the antenna elements and the point being imaged.

This result shows that the azimuth (or along-track) surface resolution is equal to half the size of the physical antenna and is independent of the distance between the sensor and the surface. At first glance, this result seems most unusual. It shows that a smaller antenna gives better resolution. This can be explained in the following way. The smaller the physical antenna is, the larger its footprint. This allows a longer observation time for each point on the surface; that is, a longer array can be synthesized. This longer synthetic array allows a finer synthetic beam and surface resolution. Similarly, if the range between the sensor and surface increases, the physical footprint increases, leading to a longer synthetic array and finer angular resolution which counterbalances the increase in the range.

As the synthetic array gets larger, it becomes necessary to compensate for the slight changes in geometry when a point is observed (Fig. 6). It should also be taken into account that the distance between the sensor and the target is variable depending on the position in the array. Thus, an additional phase shift needs to be added in the processor to the echo received at location x_i equal to

$$\phi_i = 2k(R_0 - R_i) = \frac{4\pi}{\lambda}(R_0 - R_i) \tag{28}$$

where R_0 is the range at closest approach to the point being imaged. In order to focus at a different point, a different set of phase shift corrections needs to be used. However, because this is done at a later time in the processor, optimum focusing can be achieved for each and every point in the scene. SAR imaging systems that fully apply these corrections are called *focused.*

In order to keep the processing simple, one can shorten the synthetic array length and use only a fraction of the maximum possible length. In addition, the same phase shift correction can be applied to all the echoes. This would lead to constructive addition if the partial array length is such that

$$\phi_i \le \frac{\pi}{4}$$

or

$$2k\left\{\sqrt{R^2 + \left(\frac{L'}{2}\right)^2} - R\right\} \le \frac{\pi}{4} \tag{29}$$

For large ranges, this reduces to

$$L' \le \sqrt{\frac{\lambda R}{2}} \tag{30}$$

and the achievable azimuth resolution is

$$x_a \ge \sqrt{2\lambda R} \tag{31}$$

This is called an *unfocused* SAR configuration where the azimuth resolution is somewhat degraded relative to the fully focused one, but still better than that of a real aperture radar. The advantage of the unfocused SAR is that the processing is fairly simple compared to that of a fully focused SAR.

To illustrate, for a 12 m antenna, a wavelength of 3 cm, and a platform altitude of 800 km, the azimuth resolutions will be 6 m, 220 m, and 2000 m for the cases of a fully focused SAR, an unfocused SAR, or a real aperture radar, respectively.

Doppler Synthesis Approach. Another way to explain the synthetic aperture technique is to examine the Doppler shifts of the radar signals. As the radar sensor moves relative to the target being illuminated, the backscattered echo is shifted in frequency due to the Doppler effect. This Doppler frequency is equal to

$$f_{\mathrm{d}} = 2\frac{v}{c} f_0 \cos\Psi = 2\frac{v}{\lambda}\sin\theta_{\mathrm{t}} \tag{32}$$

where f_0 is the transmitted signal frequency, Ψ is the angle between the velocity vector $\boldsymbol{v} = v\hat{\boldsymbol{v}}$ and the sensor-target line, and $\theta_{\mathrm{t}} = \pi/2 - \Psi$. As the target moves through the beam, the angle θ_{t} varies from $+\theta_{\mathrm{a}}/2$ to $-\theta_{\mathrm{a}}/2$ where θ_{a} is the antenna azimuth beamwidth. Thus, a well-defined Doppler history is associated with every target. Figure 7 shows such a history

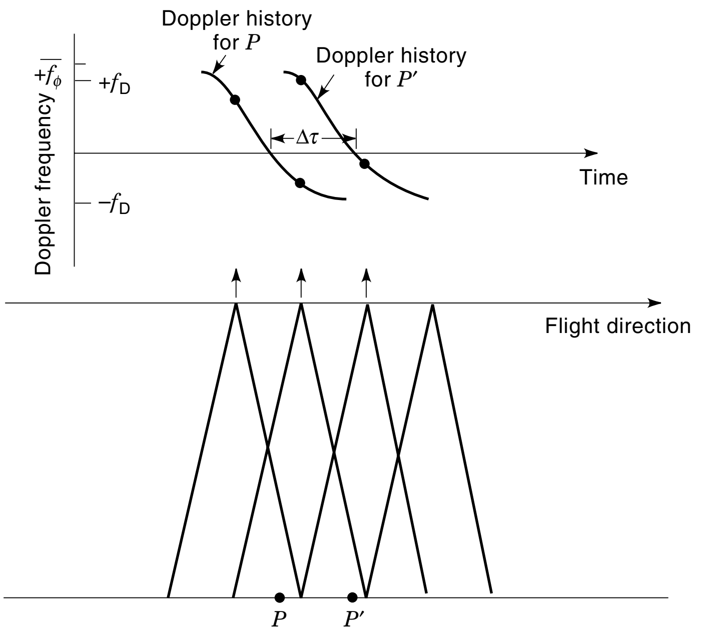

Figure 7. Doppler history for two targets separated in the azimuth direction.

for two neighboring targets P and P' located at the same range but at different azimuth positions. The Doppler shift varies from $+f_D$ to $-f_D$ where

$$f_D = 2\frac{v}{\lambda}\sin(\theta_a/2) \tag{33}$$

When $\theta_a \ll 1$, Eq. (28) can be written as

$$f_D = 2\frac{v}{\lambda}\frac{\theta_a}{2} = 2\frac{v}{\lambda}\frac{\lambda}{2L} = \frac{v}{L} \tag{34}$$

The instantaneous Doppler shift is given by

$$f_D(t) = 2\frac{v}{\lambda}\theta_t \approx 2\frac{v^2 t}{\lambda h}\cos\theta \tag{35}$$

where $t = 0$ corresponds to the time when the target is exactly at 90° to the flight track. Thus, the Doppler histories for the two points P and P' will be identical except for a time displacement equal to

$$\Delta t = \frac{PP'}{v} \tag{36}$$

It is this time displacement that allows the separation of the echoes from each of the targets.

The resolution along track (azimuth resolution) x_a is equal to the smallest separation PP' that leads to a time separation Δt that is measurable with the imaging sensor. It can be shown that this time separation is equal to the inverse of the total Doppler bandwidth $B_D = 2f_D$. In a qualitative way, it can be stated that a large B_D gives a longer Doppler history that can be better matched to a template. This would allow a better determination of the zero Doppler crossing time. Thus, the azimuth resolution is given by

$$x_a = (PP')_{\min} = v\Delta t_{\min} = v\left(\frac{1}{2f_D}\right) = v\left(\frac{L}{2v}\right) = \frac{L}{2} \tag{37}$$

which is the same as the result derived using the synthetic array approach [see Eq. (27)].

As mentioned earlier, the imaging radar transmits a series of pulsed electromagnetic waves. Thus, the Doppler history from a point P is not measured continuously but sampled on a repetitive basis. In order to get an accurate record of the Doppler history, the Nyquist sampling criterion requires that sampling occur at least at twice the highest frequency in the Doppler shift. Thus, the pulse repetition frequency (PRF), must be larger than

$$\text{PRF} \geq 2f_D = \frac{2v}{L} \tag{38}$$

In other terms, the above equation means that at least one sample (i.e., one pulse) should be taken every time the sensor moves by half an antenna length. The corresponding aspect in the synthetic array approach is that the array elements should be close enough to each other to have a reasonably "filled" total aperture in order to avoid significant grating effects. To illustrate, for a spaceborne imaging system moving at a speed of 7 km/s and using an antenna 10 m in length, the corresponding minimum PRF is 1.4 kHz.

Signal Fading and Speckle

A close examination of a synthetic-aperture radar image shows that the brightness variation is not smooth but has a granular texture which is called *speckle* (Fig. 8). Even for an imaged scene which has a constant backscatter property, the image will have statistical variations of the brightness on a pixel-by-pixel basis but will have a constant mean over many pixels. This effect is identical to when a scene is observed optically under laser illumination. It is a result of the coherent nature (or very narrow spectral width) of the illuminating signal.

To explain this effect in a simple way, let us consider a scene which is completely "black" except for two identical bright targets separated by a distance d. The received signal V at the radar is given by

$$V = V_0 e^{-i2kr_1} + V_0 e^{-i2kr_2} \tag{39}$$

and assuming that $d \ll r_0$ (for spaceborne radars, the pixel size is typically on the order of tens of meters, while the range is typically several hundred kilometers), we obtain

$$V = V_0 e^{-i2kr_0}(e^{-i2kd\sin\theta} + e^{+i2kd\sin\theta}) \Rightarrow |V| = 2|V_0\cos(kd\sin\theta)| \tag{40}$$

which shows that, depending on the exact location of the sensor, a significantly different signal value would be measured. If we now consider an image pixel which consists of a very large number of point targets, the resulting coherent superposition of all the patterns will lead to a "noise-like" signal. Rigorous mathematical analysis shows that the resulting signal has well-defined statistical properties (1–3). The measured

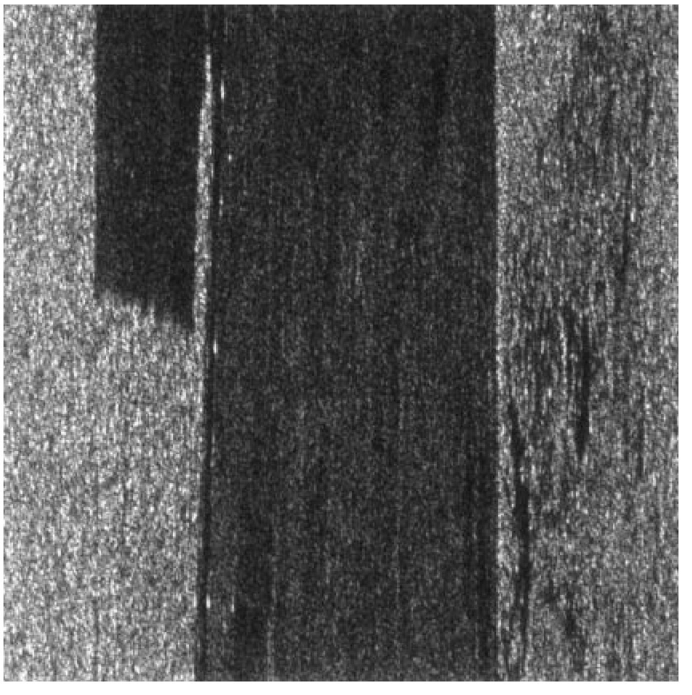

Figure 8. The granular texture shown in this image acquired by the NASA/JPL AIRSAR system is known as speckle. Speckle is a consequence of the coherent nature in which a synthetic aperture radar acquires images.

signal amplitude has a Rayleigh distribution, and the signal power has an exponential distribution (2). In order to narrow the width of these distributions (i.e., reduce the brightness fluctuations), successive signals or neighboring pixels can be averaged incoherently. This would lead to a more accurate radiometric measurement (and a more pleasing image) at the expense of degradation in the image resolution.

Another approach to reduce speckle is to combine images acquired at neighboring frequencies. In this case the exact interference patterns lead to independent signals but with the same statistical properties. Incoherent averaging would then result in a smoothing effect. In fact, this is the reason why a scene illuminated with white light does not show speckled image behavior.

In most imaging SARs, the smoothing is done by averaging the brightness of neighboring pixels in azimuth, or range, or both. The number of pixels averaged is called the number of *looks* N. It can be shown (1) that the signal standard deviation S_N is related to the mean signal power $\overline{P}$ by

$$S_N = \frac{1}{\sqrt{N}}\overline{P} \tag{41}$$

The larger the number of looks N, the better the quality of the image from the radiometric point of view. However, this degrades the spatial resolution of the image. It should be noted that for N larger than about 25, large increase in N leads to only a small decrease in the signal fluctuation. This small improvement in the radiometric resolution should be traded off against the large increase in the spatial resolution. For example, if one were to average 10 resolution cells in a four-look image, the speckle noise will be reduced to about 0.5 dB. At the same time, however, the image resolution will be reduced by an order of magnitude. Whether this loss in resolution is worth the reduction in speckle noise depends on both the aim of the investigation, and the kind of scene imaged.

Figure 9 shows the effect of multilook averaging. The same image as Fig. 8, acquired by the NASA/JPL AIRSAR system, is shown displayed at one, four, 16, and 32 looks, respectively. This figure clearly illustrates the smoothing effect, as well as the decrease in resolution resulting from the multilook process. In one early survey of geologists done by Ford (4), the results showed that even though the optimum number of looks depended on the scene type and resolution, the majority of the responses preferred 2-look images. However, this survey dealt with images that had rather poor resolution to begin with; and one may well find that with today's higher-resolution systems, analysts may be asking for a larger number of looks.

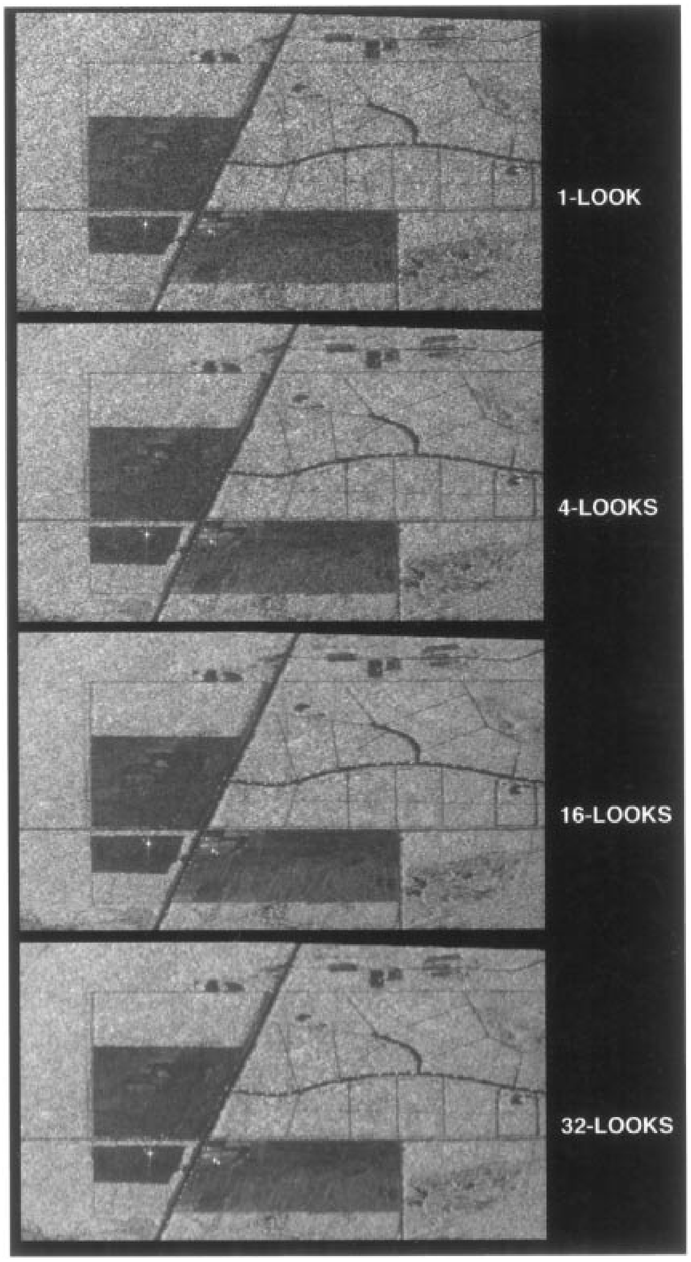

Figure 9. The effects of speckle can be reduced by incoherently averaging pixels in a radar image, a process known as multilooking. Shown in this figure is the same image, processed as a single look (the basic radar image), 4 looks, 16 looks, and 32 looks. Note the reduction in granular texture as the number of looks increase. Also, note that as the number of looks increases, the resolution of the images decreases. Some features, such as those in the largest dark patch, may be completely masked by the speckle noise.

Ambiguities and Anomalies

Radar images could contain a number of anomalies which result from the way imaging radars generate the image. Some of these are similar to what is encountered in optical systems, such as blurring due to defocusing or scene motion, and some such as range ambiguities are unique to radar systems. This section addresses the anomalies which are most commonly encountered in radar images.

As mentioned earlier (see Fig. 3) a radar images a surface by recording the echoes line by line with successive pulses. The leading edge of each echo corresponds to the near edge of the image scene, and the tail end of the echo corresponds to the far edge of the scene. The length of the echo (i.e., swath width of the scene covered) is determined by the antenna beamwidth and the size of the data window. The exact timing of the echo reception depends on the range between the sensor and the surface being imaged. If the timing of the pulses or the extent of the echo are such that the leading edge of one echo overlaps with the tail end of the previous one, then the far edge of the scene is folded over the near edge of the scene.

This is called *range ambiguity*. Referring to Fig. 10, the temporal extent of the echo is equal to

$$T_e \approx 2\frac{R}{c}\theta_r \tan\theta = 2\frac{h\lambda}{cW}\frac{\sin\theta}{\cos^2\theta} \tag{42}$$

This time extent should be shorter than the time separating two pulses (i.e., 1/PRF). Thus, we must have

$$\mathrm{PRF} < \frac{cW}{2h\lambda}\frac{\cos^2\theta}{\sin\theta} \tag{43}$$

In addition, the sensor parameters, specifically the PRF, should be selected such that the echo is completely within an interpulse period; that is, no echoes should be received during the time that a pulse is being transmitted.

The above equation gives an upper limit for the PRF. Another kind of ambiguity present in SAR imagery also results from the fact that the target's return in the azimuth direction is sampled at the PRF. This means that the azimuth spectrum of the target return repeats itself in the frequency domain at multiples of the PRF. In general, the azimuth spectrum is not a band-limited signal; instead the spectrum is weighted by the antenna pattern in the azimuth direction. This means that parts of the azimuth spectrum may be aliased, and high-frequency data will actually appear in the low-frequency part of the spectrum. In actual images, these *azimuth ambiguities* appear as ghost images of a target repeated at some distance in the azimuth direction as shown in Fig. 11. To reduce the azimuth ambiguities, the PRF of a SAR has to exceed the lower limit given by Eq. (33).

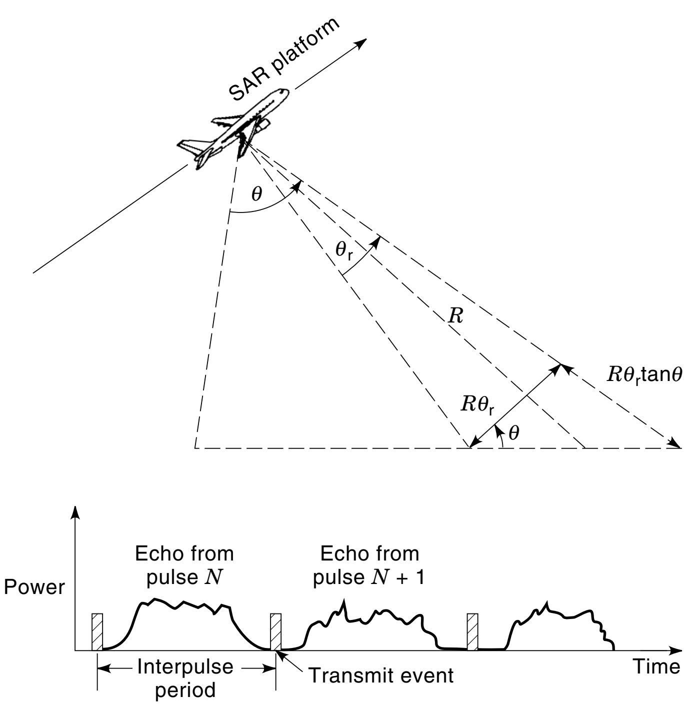

Figure 10. Temporal extent of radar echoes. If the timing of the pulses or the temporal extent of the echoes is such that the leading edge of one echo overlaps the trailing edge of the previous one, the far edge of the scene will be folded over the near edge, a phenomenon known as range ambiguities.

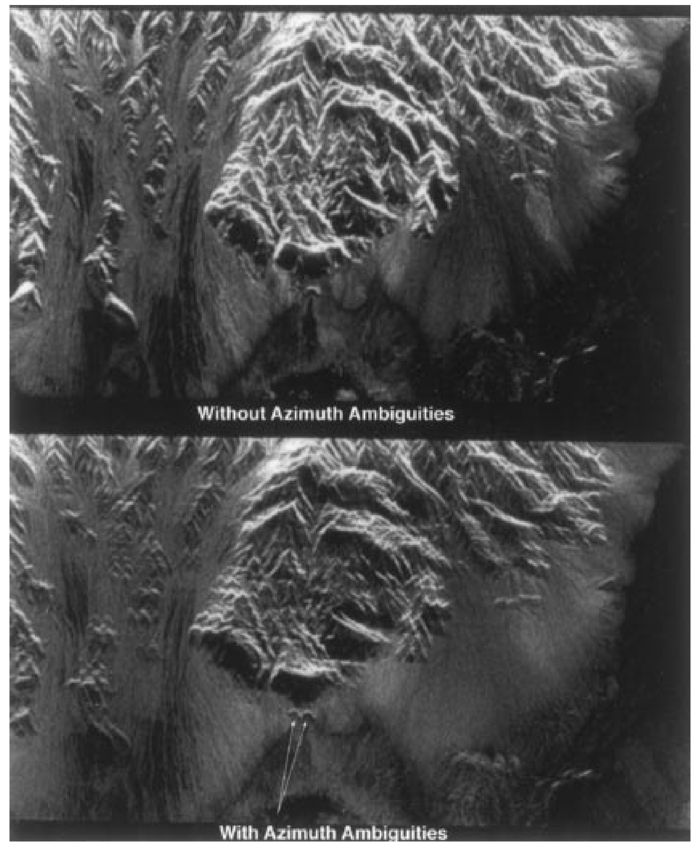

Figure 11. Azimuth ambiguities result when the radar pulse repetition frequency is too low to sample the azimuth spectrum of the data adequately. In that case, the edges of the azimuth spectrum fold over themselves, creating ghost images as shown in this figure. The top image was adequately sampled and processed, while the bottom one clearly shows the ghost images due to the azimuth ambiguities. The data were acquired with the NASA/JPL AIRSAR system, and a portion of Death Valley in California is shown.

In order to reduce both range and azimuth ambiguities, the PRF must therefore satisfy the conditions expressed by both Eqs. (33) and (43). Therefore, we must insist that

$$\frac{cW}{2h\lambda}\frac{\cos^2\theta}{\sin\theta} > \frac{2v}{L} \tag{44}$$

from which we derive a lower limit for the antenna size as

$$LW > \frac{4vh\lambda}{c}\frac{\sin\theta}{\cos^2\theta} \tag{45}$$

Another type of artifact in radar images results when a very bright surface target is surrounded by a dark area. As the image is being formed, some spillover from the bright target, called sidelobes, although weak, could exceed the background and become visible as shown in Fig. 12. It should be pointed out that this type of artifact is not unique to radar systems. They are common in optical systems, where they are known as the sidelobes of the point spread function. The difference is that in optical systems the sidelobe characteristics are determined by the characteristics of the imaging optics (i.e., the

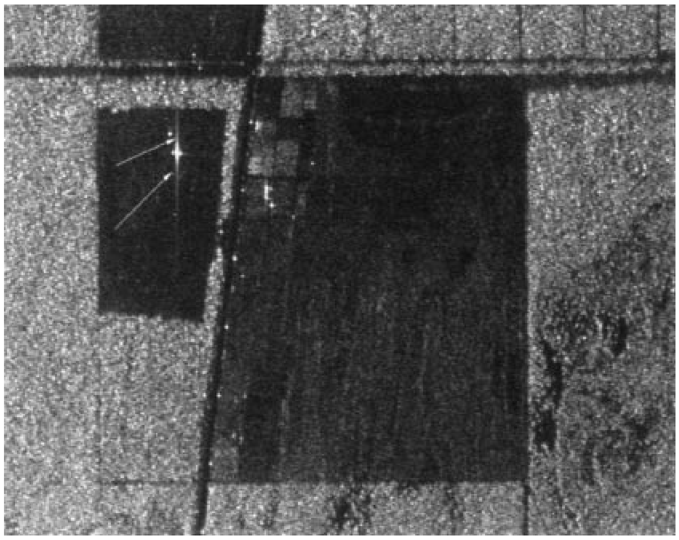

Figure 12. Sidelobes from the bright target, indicated by arrows in this image, mask out the return from the dark area surrounding the target. The characteristics of the sidelobes are determined mainly by the characteristics of the radar processing filters.

hardware), whereas in the case of a SAR the sidelobe characteristics are determined by the characteristics of the processing filters. In the radar case, the sidelobes may therefore be reduced by suitable weighting of the signal spectra during matched filter compression. The equivalent procedure in optical systems is through apodization of the telescope aperture.

The vast majority of these artifacts and ambiguities can be avoided with proper selection of the sensor's and processor's parameters. However, the interpreter should be aware of their occurrence because in some situations they might be difficult, if not impossible, to suppress.

Geometric Effects and Projections

The time delay/Doppler history basis of SAR image generation leads to an image projection different than that in the case of optical sensors. Even though at first look radar images seem very similar to optical images, close examination quickly shows that geometric shapes and patterns are projected in a different fashion by the two sensors. This difference is particularly acute in rugged terrain. If the topography is known, a radar image can be reprojected into a format identical to an optical image, thus allowing image pixel registration. In extremely rugged terrain, however, the nature of the radar image projection leads to distortions which sometimes cannot be corrected. In the radar image, two neighboring pixels in the range dimension correspond to two areas in the scene with slightly different range to the sensor. This has the effect of projecting the scene in a cylindrical geometry on the image plane, which leads to distortions as shown in Fig. 13. Areas that slope toward the sensor look shorter in the image, while areas that slope away from the sensor look longer in the image than horizontal areas. This effect is called *foreshortening*. In the extreme case where the slope is larger than the incidence angle, *layover* occurs. In this case, a hill would look as if it is projected over the region in front of it. Layover cannot be corrected and can only be avoided by having an incidence angle at the surface larger than any expected surface slopes. When the slope facing away from the radar is steep enough such that the radar waves do not illuminate it, *shadowing* occurs and the area on that slope is not imaged. Note that in the radar images, shadowing is always away from the sensor flight line and is not dependent on the time of data acquisition or the sun angle in the sky. Shadowing can be beneficial for highlighting surface morphologic patterns. Figure 14 contains some examples of foreshortening and shadowing.

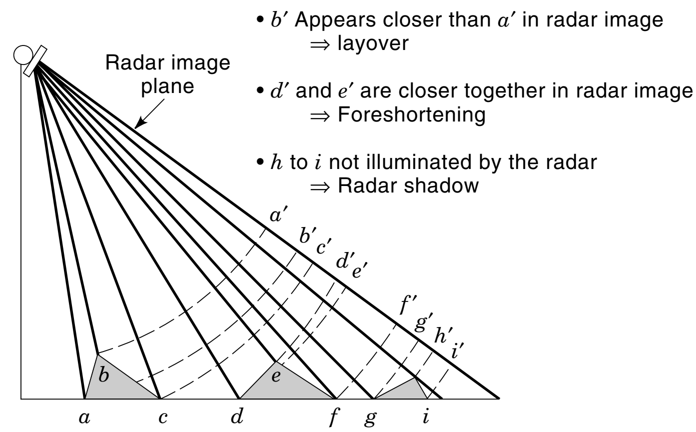

Figure 13. Radar images are cylindrical projections of the scene onto the image plane, leading to characteristic distortions. Refer to the text for more detailed discussions.

ADVANCED SAR TECHNIQUES

The field of synthetic aperture radar changed dramatically over the years, especially over the past decade with the operational introduction of advance radar techniques such as polarimetry and interferometry. While both of these techniques have been demonstrated much earlier, radar polarimetry only became an operational research tool with the introduction of the NASA/JPL AIRSAR system in the early 1980s, and it reached a climax with the two SIR-C/X-SAR flights on board

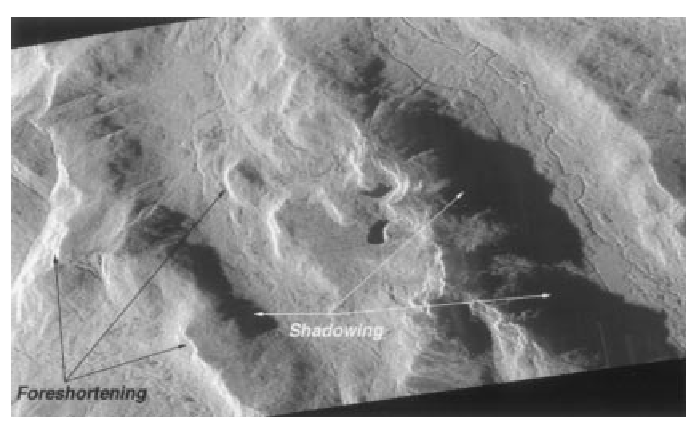

Figure 14. This NASA/JPL AIRSAR image shows examples of foreshortening and shadowing. Note that since the radar provides its own illumination, radar shadowing is a function of the radar look direction and does not depend on the sun angle. This image was illuminated from the left.

the space shuttle Endeavour in April and October 1994. Radar interferometry received a tremendous boost when the airborne TOPSAR system was introduced in 1991 by NASA/JPL, and it progressed even further when data from the European Space Agency ERS-1 radar satellite became routinely available in 1991.

SAR Polarimetry

Radar polarimetry is covered in detail in a different article in this encyclopedia. We therefore only summarize this technique here for completeness. The reader is referred to the appropriate article in this encyclopedia for the mathematical details.

Electromagnetic wave propagation is a vector phenomenon; that is, all electromagnetic waves can be expressed as complex vectors. Plane electromagnetic waves can be represented by two-dimensional complex vectors. This is also the case for spherical waves when the observation point is sufficiently far removed from the source of the spherical wave. Therefore, if one observes a wave transmitted by a radar antenna when the wave is a large distance from the antenna (in the far-field of the antenna), the radiated electromagnetic wave can be adequately described by a two-dimensional complex vector. If this radiated wave is now scattered by an object, and one observes this wave in the far-field of the scatterer, the scattered wave can again be adequately described by a two-dimensional vector. In this abstract way, one can consider the scatterer as a mathematical operator which takes one two-dimensional complex vector (the wave impinging upon the object) and changes it into another two-dimensional vector (the scattered wave). Mathematically, therefore, a scatterer can be characterized by a complex 2×2 scattering matrix. However, this matrix is a function of the radar frequency, and the viewing geometry. Once the complete scattering matrix is known and calibrated, one can synthesize the radar cross-section for any arbitrary combination of transmit and receive polarizations. Figure 15 shows a number of such synthesized images for the San Francisco Bay area in California. The data were acquired with the NASA/JPL AIRSAR system.

The typical implementation of a radar polarimeter involves transmitting a wave of one polarization and receiving echoes in two orthogonal polarizations simultaneously. This is followed by transmitting a wave with a second polarization, and again receiving echoes with both polarizations simultaneously. In this way, all four elements of the scattering matrix are measured. This implementation means that the transmitter is in slightly different positions when measuring the two columns of the scattering matrix, but this distance is typically small compared to a synthetic aperture and therefore does not lead to a significant decorrelation of the signals. The NASA/JPL AIRSAR system pioneered this implementation for SAR systems (5), and the same implementation was used in the SIR-C part of the SIR-C/X-SAR radars (6).

The past few years have seen relatively little advance in the development of hardware for polarimetric SAR systems; newer implementations are simply using more advanced technology to implement the same basic hardware configurations as the initial systems. Significant advances were made, however, in the field of analysis and application of polarimetric SAR data.

Polarimetric SAR Calibration. Many of the advances made in analyzing polarimetric SAR data result directly from the greater availability of calibrated data. Unlike the case of single-channel radars, where only the radar cross section needs to be calibrated, polarimetric calibration usually involves four steps: cross-talk removal, phase calibration, channel imbalance compensation, and absolute radiometric calibration (7). Cross-talk removal refers to correcting mostly the cross-polarized elements of the scattering matrix for the effects of system cross-talk that couples part of the copolarized returns into the cross-polarized channel. Phase calibration refers to correcting the copolarized phase difference for uncompensated path length differences in the transmit and receive chains, while channel imbalance refers to balancing the copolarized and cross-polarized returns for uncompensated gain differences in the two transmit and receive chains. Finally, absolute radiometric calibration involves using some kind of a reference calibration source to determine the overall system gain to relate received power levels to normalized radar cross section.

While most of the polarimetric calibration algorithms currently in use were published several years ago (7–11), several groups are still actively pursuing the study of improved calibration techniques and algorithms. The earlier algorithms are reviewed in Refs. 12 and 13, while Ref. 14 provides a comprehensive review of SAR calibration in general. Some of these earlier algorithms are now routinely used to calibrate polarimetric SAR data operationally, as for example in the NASA/JPL AIRSAR and SIR-C processors (15).

Example Applications of Polarimetric SAR Data. The availability of calibrated polarimetric SAR data allowed research to move from the qualitative interpretation of SAR images to the quantitative analysis of the data. This sparked significant progress in the classification of polarimetric SAR images, led to improved models of scattering by different types of terrain, and allowed the development of some algorithms to invert polarimetric SAR data for geophysical parameters, such as forest biomass, surface roughness, and soil moisture.

Classification of Earth Terrain. Many earth science studies require information about the spatial distribution of land cover types, as well as the change in land cover and land use with time. In addition, it is increasingly recognized that the inversion of SAR data for geophysical parameters involves an initial step of segmenting the image into different terrain classes, followed by inversion using the algorithm appropriate for the particular terrain class. Polarimetric SAR systems, capable of providing high-resolution images under all weather conditions as well as during day or night, provide a valuable data source for classification of earth terrain into different land cover types.

Two main approaches are used to classify images into land cover types: (1) maximum likelihood classifiers based on Bayesian statistical analysis and (2) knowledge-based techniques designed to identify dominant scattering.

Some of the earlier studies in Bayesian classification focused on quantifying the increased accuracy gained from using all the polarimetric information. References 16 and 17 showed that the classification accuracy is significantly increased when the complete polarimetric information is used compared to that achieved with single-channel SAR data. These earlier classifiers assumed equal a priori probabilities for all classes, and modeled the SAR amplitudes as circular

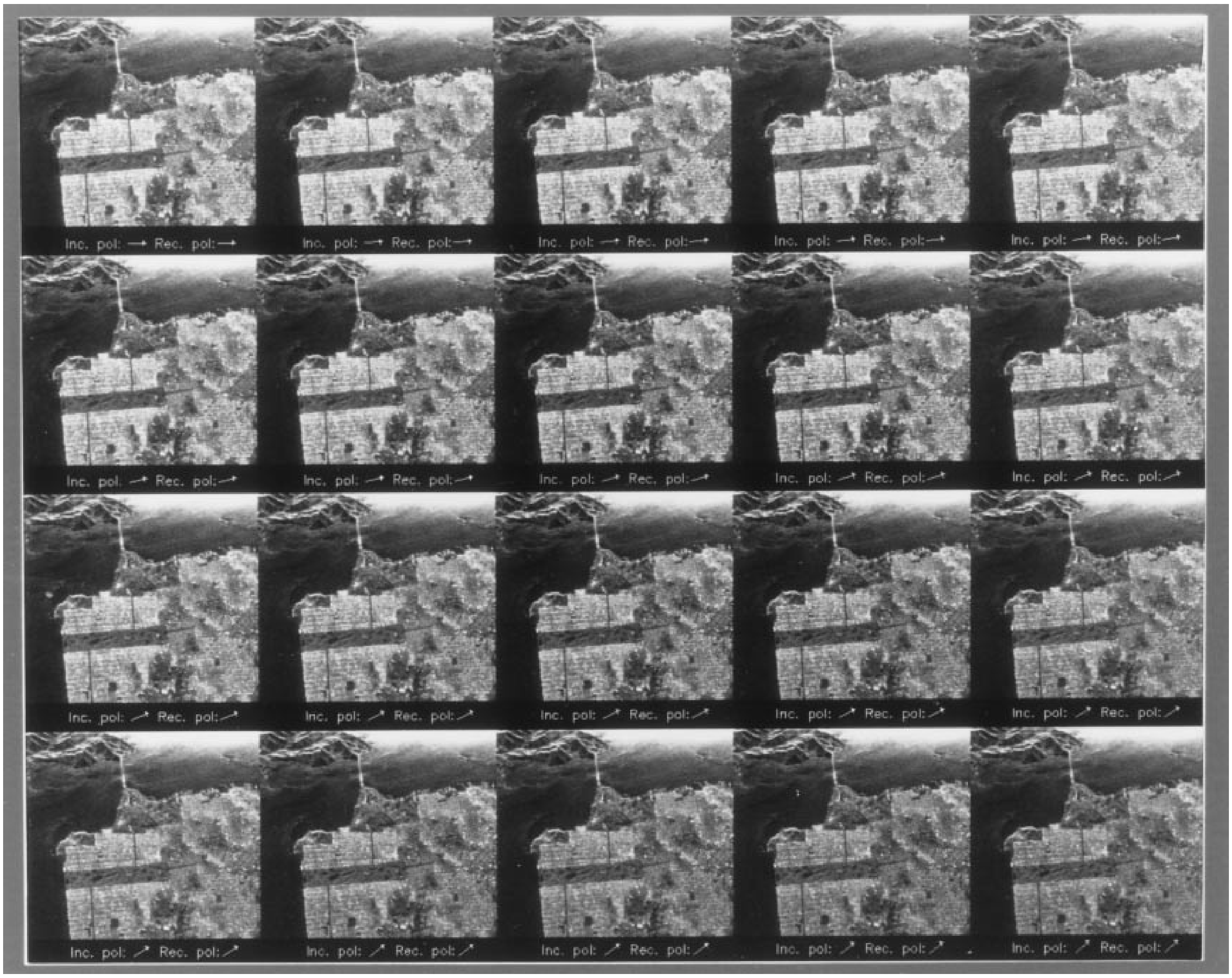

Figure 15. Radar polarimetry allows one to synthesize images at any polarization combination. This set of images of San Francisco, California, was synthesized from a single set of measurements acquired by the NASA/JPL AIRSAR system. Note the differential change in brightness between the city (the bright area) and Golden Gate Park, the dark rectangular area in the middle of the images. This differential change is due to a difference in scattering mechanism. The city area is dominated by a double reflection from the streets to the buildings and back to the radar, while the park area exhibits much more diffuse scattering.

Gaussian distributions, which means that the textural variations in radar backscatter are not considered to be significant enough to be included in the classification scheme. Reference 18 extended the Bayesian classification to allow different a priori probabilities for different classes. Their method first classifies the image into classes assuming equal a priori probabilities, and then it iteratively changes the a priori probabilities for subsequent classifications based on the local results of previous classification runs. Significant improvement in classification accuracy is obtained with only a few iterations. More accurate results are obtained using a more rigorous maximum a posteriori (MAP) classifier where the a priori distribution of image classes is modeled as a Markov random field and the optimization of the image classes is done over the whole image instead of on a pixel-by-pixel basis (19). In a subsequent work, the MAP classifier is extended to include the case of multifrequency polarimetric radar data (20). The MAP classifier was used in Ref. 21 to map forest types in the Alaskan boreal forest. In this study, five vegetation types (white spruce, balsam poplar, black spruce, alder/willow shrubs, and bog/fen/nonforest) were separated with accuracies ranging from 62% to 90%, depending on which frequencies and polarizations are used.

Knowledge-based classifiers are implemented based upon determination of dominant scattering mechanisms through an understanding of the physics of the scattering process as well as experience gained from extensive experimental measurements (22). One of the earliest examples of such a knowledge-based classifier was published in Ref. 23. In this unsupervised classification, knowledge of the physics of the scattering process was used to classify images into three classes: odd numbers of reflections, even numbers of reflections, and diffuse scattering. The odd and even numbers of reflection classes are separated based on the copolarized phase difference, while the diffuse scattering class is identified based on high cross-polarized return and low correlation between the copolarized channels. While no direct attempt was made to identify each class with a particular terrain type, it was noted that in most cases the odd numbers of reflection class corresponded to bare surfaces or open water, even numbers of reflections usually indicated urban areas or sparse forests, sometimes with understory flooding present, and diffuse scattering is usually identified with vegetated areas. As such, all vegetated areas are lumped into one class, restricting the application of the results. Reference 22 extended this idea and developed a level 1 classifier that segments images into four classes: tall vegetation (trees), short vegetation, urban surfaces, and bare surfaces. First the urban areas are separated from the rest by using the L-band copolarized phase difference and the image texture at C-band. Then areas containing tall vegetation are identified using the L-band cross-polarized return. Finally, the C-band cross-polarized return and the L-band texture are used to separate the areas containing short vegetation from those with bare surfaces. Accuracies better than 90% are reported for this classification scheme when applied to two different images acquired in Michigan. Another example of a knowledge-based classification is reported in Ref. 24. In this study, a decision-tree classifier is used to classify images of the Amazonian floodplain near Manaus, Brazil into five classes: water; clearing; macrophyte; nonflooded forest; and flooded forest based on polarimetric scattering properties. Accuracies better than 90% are reported.

Geophysical Parameter Estimation. One of the most active areas of research in polarimetric SAR involves estimating geophysical parameters directly from the radar data through model inversion. Space does not permit a full discussion of recent work. Therefore, in this section only a brief summary of recent work will be provided, with the emphasis on vegetated areas.

Many electromagnetic models exist to predict scattering from vegetated areas (25–34), and this remains an area of active research. Much of the work is aimed at estimating forest biomass (35–39). Earlier works correlated polarimetric SAR backscatter with total above-ground biomass (35,36) and suggested that the backscatter saturates at a biomass level that scales with frequency, a result also predicted by theoretic models. This led some investigators to conclude that these saturation levels define the upper limits for accurate estimation of biomass (40), arguing for the use of low-frequency radars to be used for monitoring forest biomass (41).

More recent work suggests that some spectral gradients and polarization ratios do not saturate as quickly and may therefore be used to extend the range of biomass levels for which accurate inversions could be obtained (37). Reference 41 showed that inversion results are most accurate for monospecies forests, and it also showed that accuracies decrease for less homogeneous forests. They conclude that the accuracies of the radar estimates of biomass are likely to increase if structural differences between forest types are accounted for during the inversion of the radar data.

Such an integrated approach to retrieval of forest biophysical characteristics is reported in Refs. 42 and 43. These studies first segment images into different forest structural types, and then they use algorithms appropriate for each structural type in the inversion. Furthermore, Ref. 43 estimates the total biomass by first using the radar data to estimate tree basal area and height and crown biomass. The tree basal area and height are then used in allometric equations to estimate the trunk biomass. The total biomass, which is the sum of the trunk and crown biomass values, is shown to be accurately related to allometric total biomass levels up to 25 kg/m^2, while Ref. 44 estimates that biomass levels as high as 34 kg/m^2 to 40 kg/m^2 could be estimated with an accuracy of 15% to 25% using multipolarization C-, L-, and P-band SAR data.

Research in retrieving geophysical parameters from nonvegetated areas is also an active research area, although not as many groups are involved. One of the earliest algorithms to infer soil moisture and surface roughness for bare surfaces was published in Ref. 45. This algorithm uses polarization ratios to separate the effects of surface roughness and soil moisture on the radar backscatter, and an accuracy of 4% for soil moisture is reported. More recently, Dubois et al. (46) reported a slightly different algorithm, based only on the copolarized backscatters measured at the L-band. Their results, using data from scatterometers, airborne SARs, and spaceborne SARs (SIR-C), show an accuracy of 4.2% when inferring soil moisture over bare surfaces. Reference 47 reported an algorithm to measure snow wetness, and it demonstrated accuracies of 2.5%.

SAR Interferometry

SAR interferometry refers to a class of techniques where additional information is extracted from SAR images that are acquired from different vantage points, or at different times. Various implementations allow different types of information to be extracted. For example, if two SAR images are acquired from slightly different viewing geometries, information about the topography of the surface can be inferred. On the other hand, if images are taken at slightly different times, a map of surface velocities can be produced. Finally, if sets of interferometric images are combined, subtle changes in the scene can be measured with extremely high accuracy.

In this section we shall first discuss so-called cross-track interferometers used for the measurement of surface topography. This will be followed by a discussion of along-track interferometers used to measure surface velocity. The section ends with a discussion of differential interferometry used to measure surface changes and deformation.

Radar Interferometry for Measuring Topography. SAR interferometry was first demonstrated by Graham (48), who demonstrated a pattern of nulls or interference fringes by vectorally adding the signals received from two SAR antennas, one physically situated above the other. Later, Zebker and Goldstein (49) demonstrated that these interference fringes can be formed after SAR processing of the individual images if both the amplitude and the phase of the radar images are preserved during the processing.

The basic principles of interferometry can be explained using the geometry shown in Fig. 16. Using the law of cosines on the triangle formed by the two antennas and the point being imaged, it follows that

$$(R + \delta R)^2 = R^2 + B^2 - 2BR \cos\left(\frac{\pi}{2} - \theta + \alpha\right) \qquad (46)$$

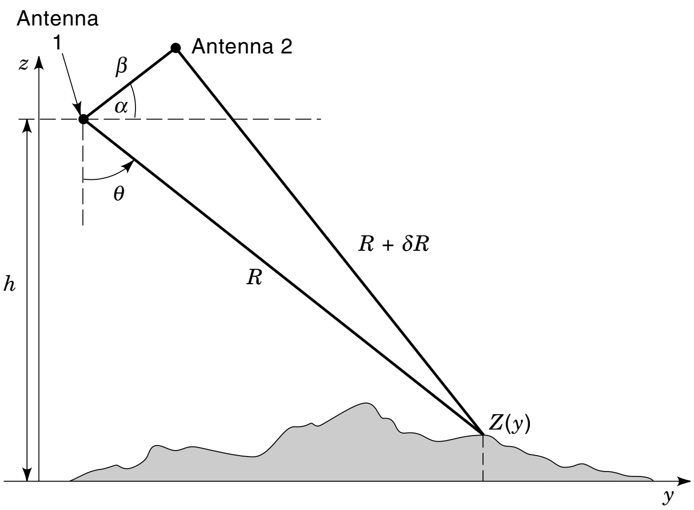

Figure 16. Basic interferometric radar geometry. The path length difference between the signals measured at each of the two antennas is a function of the elevation of the scatterer.

where R is the slant range to the point being imaged from the reference antenna, δR is the path length difference between the two antennas, B is the physical interferometric baseline length, θ is the look angle to the point being imaged, and α is the baseline tilt angle with respect to the horizontal.

From Eq. (46) it follows that we can solve for the path length difference δR. If we assume that $R \gg B$ (a very good assumption for most interferometers), one finds that

$$\delta R \approx -B \sin(\theta - \alpha) \tag{47}$$

The radar system does not measure the path length difference explicitly, however. Instead, what is measured is an interferometric phase difference that is related to the path length difference through

$$\phi = \frac{a2\pi}{\lambda}\delta R = -\frac{a2\pi}{\lambda} B \sin(\theta - \alpha) \tag{48}$$

where $a = 1$ for the case where signals are transmitted out of one antenna and received through both at the same time, and $a = 2$ for the case where the signal is alternately transmitted *and received* through one of the two antennas only. The radar wavelength is denoted by λ.

From Fig. 16, it also follows that the elevation of the point being imaged is given by

$$z(y) = h - R\cos\theta \tag{49}$$

with h denoting the height of the imaging reference antenna above the reference plane with respect to which elevations are quoted. From Eq. (48) one can infer the actual radar look angle from the measured interferometric phase as

$$\theta = \alpha - \sin^{-1}\left(\frac{\lambda\phi}{a2\pi B}\right) \tag{50}$$

Using Eqs. (50) and (49), one can now express the inferred elevation in terms of system parameters and measurables as

$$z(y) = h - R\cos\left(\alpha - \sin^{-1}\left(\frac{\lambda\phi}{a2\pi B}\right)\right) \tag{51}$$

This expression is the fundamental IFSAR equation for broadside imaging geometry.

SAR interferometers for the measurement of topography can be implemented in one of two ways. In the case of single-pass interferometry, the system is configured to measure the two images at the same time through two different antennas usually arranged one above the other. The physical separation of the antennas is referred to as the baseline of the interferometer. In the case of repeat-track interferometry, the two images are acquired by physically imaging the scene at two different times using two different viewing geometries.

So far all single-pass interferometers have been implemented using airborne SARs (49–51). The Shuttle Radar Topography Mission (SRTM), a joint project between the United States National Imagery and Mapping Agency (NIMA) and the National Aeronautics and Space Administration (NASA), will be the first spaceborne implementation of a single pass interferometer (52). Scheduled for launch in 1999, SRTM will use modified hardware from the C-band radar of the SIR-C system, with a 62-m-long boom and a second antenna to form a single-pass interferometer. The SRTM mission will acquire digital topographic data of the globe between 60° north and south latitudes during one 11-day shuttle mission. The SRTM mission will also acquire interferometric data using modified hardware from the X-band part of the SIR-C/X-SAR system. The swaths of the X-band system, however, are not wide enough to provide global coverage during the mission.

Most of the SAR interferometry research has gone into understanding the various error sources and how to correct their effects during and after processing. As a first step, careful motion compensation must be performed during processing to correct for the actual deviation of the aircraft platform from a straight trajectory (53). As mentioned before, the single-look SAR processor must preserve both the amplitude and the phase of the images. After single-look processing, the images are carefully co-registered to maximize the correlation between the images. The so-called interferogram is formed by subtracting the phase in one image from that in the other on a pixel-by-pixel basis.

The interferometric SAR technique is better understood by briefly reviewing the difference between traditional and interferometric SAR processing. In traditional (noninterferometric) SAR processing, it is assumed that the imaged pixel is located at the intersection of the Doppler cone (centered on the velocity vector), the range sphere (centered at the antenna), and an assumed reference plane, as shown in Fig. 17. Since the Doppler cone has its apex at the center of the range sphere, and its axis of symmetry is aligned with the velocity vector, it follows that all points on the intersection of the Doppler cone and the range sphere lie in a plane orthogonal to the velocity vector.

The additional information provided by cross-track interferometry is that the imaged point also has to lie on the cone described by a constant phase, which means that one no longer has to assume an arbitrary reference plane. This cone of equal phase has its axis of symmetry aligned with the interferometer baseline and also has its apex at the center of the range sphere. It then follows that the imaged point lies at the intersection of the Doppler cone, the range sphere, and the equal phase cone, as shown in Fig. 18. It should be pointed out that in actual interferometric SAR processors, the two images acquired by the two interferometric antennas are

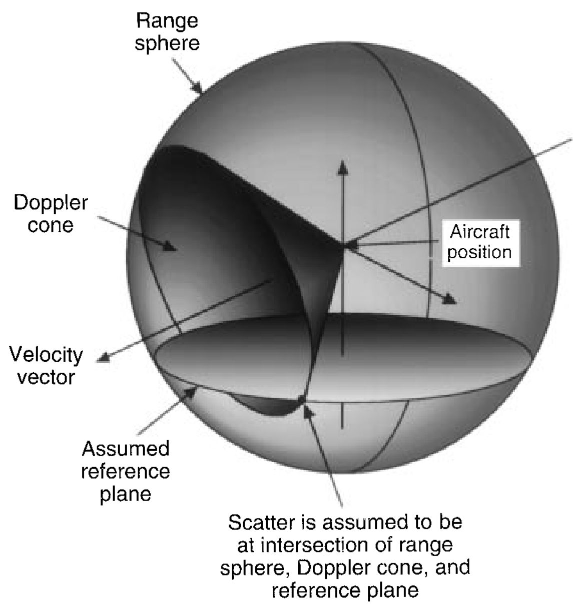

Figure 17. In traditional (noninterferometric) SAR processing, the scatterer is assumed to be located at the intersection of the Doppler cone, the range sphere, and some assumed reference plane.

actually processed individually using the traditional SAR processing assumptions. The resulting interferometric phase then represents the elevation with respect to the reference plane assumed during the SAR processing. This phase is then used to find the actual intersection of the range sphere, the Doppler cone, and the phase cone in three dimensions.

Once the images are processed and combined, the measure phase must be *unwrapped.* During this procedure, the measured phase, which only varies between 0° and 360°, must be

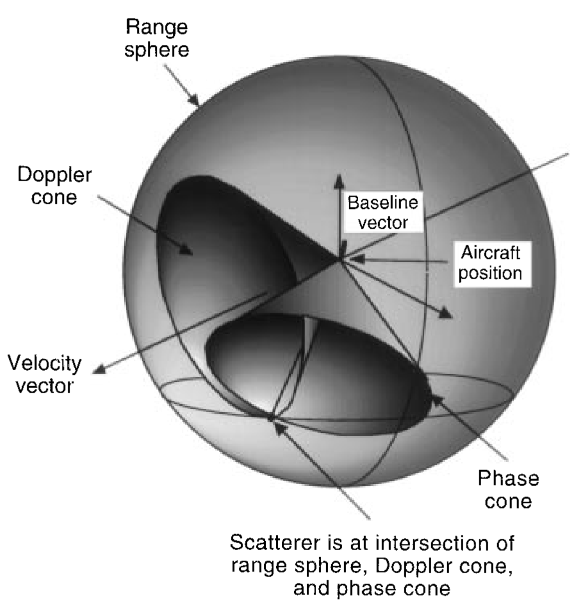

Figure 18. Interferometric radars acquire all the information required to reconstruct the position of a scatterer in three dimensions. The scatterer is located at the intersection of the Doppler cone, the range sphere, and the interferometric phase cone.

unwrapped to retrieve the original phase by adding or subtracting multiples of 360°. The earliest phase unwrapping routine was published by Goldstein et al. (54). In this algorithm, areas where the phase will be discontinuous due to layover or poor SNRs are identified by branch cuts, and the phase unwrapping routine is implemented such that branch cuts are not crossed when unwrapping the phases. Phase unwrapping remains one of the most active areas of research, and many algorithms remain under development.

Even after the phases have been unwrapped, the absolute phase is still not known. This absolute phase is required to produce a height map that is calibrated in the absolute sense. One way to estimate this absolute phase is to use ground control points with known elevations in the scene. However, this human intervention severely limits the ease with which interferometry can be used operationally. Madsen et al. (53) reported a method by which the radar data are used to estimate this absolute phase. The method breaks the radar bandwidth up into upper and lower halves, and then it uses the differential interferogram formed by subtracting the upper half spectrum interferogram from the lower half spectrum interferogram to form an equivalent low-frequency interferometer to estimate the absolute phase. Unfortunately, this algorithm is not robust enough in practice to fully automate interferometric processing. This is one area where significant research is needed if the full potential of automated SAR interferometry is to be realized.

Absolute phase determination is followed by height reconstruction. Once the elevations in the scene are known, the entire digital elevation map can be geometrically rectified. Reference 53 reported accuracies ranging between 2.2 m root mean square (rms) for flat terrain and 5.5 m rms for terrain with significant relief for the NASA/JPL TOPSAR interferometer.

An alternative way to form the interferometric baseline is to use a single-channel radar to image the same scene from slightly different viewing geometries. This technique, known as *repeat-track* interferometry, has been mostly applied to spaceborne data starting with data collected with the L-band SEASAT SAR (54–59). Other investigators used data from the L-band SIR-B (60), the C-band ERS-1 radar (61,62), and more recently the L-band SIR-C (63) and the X-band X-SAR (64). Repeat-track interferometry has also been demonstrated using airborne SAR systems (65).

Two main problems limit the usefulness of repeat-track interferometry. The first is due to the fact that, unlike the case of single-pass interferometry, the baseline of the repeat-track interferometer is not known accurately enough to infer accurate elevation information from the interferogram. Reference 62 shows how the baseline can be estimated using ground control points in the image. The second problem is due to differences in scattering and propagation that results from the fact that the two images forming the interferogram are acquired at different times. One result is temporal decorrelation, which is worst at the higher frequencies (58). For example, C-band images of most vegetated areas decorrelate significantly over as short a time as 1 day. This problem, more than any other, limits the use of the current operational spaceborne single-channel SARs for topographic mapping, and it has led to proposals for dedicated interferometric SAR missions to map the entire globe (66,67).

Along-Track Interferometry. In some cases, the temporal change between interferometric image contains much information. One such case is the mapping of ocean surface movement. In this case, the interferometer is implemented in such a way that one antenna images the scene a short time before the second antenna, preferably using the same viewing geometry. Reference 68 described such an implementation in which one antenna is mounted forward of the other on the body of the NASA DC-8 aircraft. In a later work, Ref. 69 measured ocean currents with a velocity resolution of 5 m/s to 10 m/s. Along-track interferometry was used by Refs. 70 and 71 to estimate ocean surface current velocity and wavenumber spectra. This technique was also applied to the measurement of ship-generated internal wave velocities by Ref. 72.

In addition to measuring ocean surface velocities, Carande (73) reported a dual baseline implementation, implemented by alternately transmitting out of the front and aft antennas, to measure ocean coherence time. He estimated typical ocean coherence times for the L-band to be about 0.1 s. Shemer and Marom (74) proposed a method to measure ocean coherence time using only a model for the coherence time and one interferometric SAR observation.

Differential Interferometry. One of the most exciting applications of radar interferometry is implemented by subtracting two interferometric pairs separated in time from each other to form a so-called differential interferogram. In this way, surface deformation can be measured with unprecedented accuracy. This technique was first demonstrated by Gabriel et al. (75) using data from SEASAT data to measure millimeter-scale ground motion in agricultural fields. Since then this technique has been applied to measure centimeter- to meter-scale co-seismic displacements (76–81) and to measure centimeter-scale volcanic deflation (82). The added information provided by high-spatial-resolution co-seismic deformation maps was shown to provide insight into the slip mechanism that would not be attainable from the seismic record (79,80).

Differential SAR interferometry has also led to spectacular applications in polar ice sheet research by providing information on ice deformation and surface topography at an unprecedented level of spatial details. Goldstein et al. (83) observed ice stream motion and tidal flexure of the Rutford Glacier in Antarctica with a precision of 1 mm per day and summarized the key advantages of using SAR interferometry for glacier studies. Joughin (84) studied the separability of ice motion and surface topography in Greenland and compared the results with both radar and laser altimetry. Rignot et al. (85) estimated the precision of the SAR-derived velocities using a network of *in situ* velocities and demonstrated, along with Joughin et al. (86), the practicality of using SAR interferometry across all the different melting regimes of the Greenland Ice Sheet. Large-scale applications of these techniques is expected to yield significant improvements in our knowledge of the dynamics, mass balance, and stability of the world's major ice masses.

One confusing factor in the identification of surface deformation in differential interferograms is due to changing atmospheric conditions. In observing the earth, radar signals propagate through the atmosphere, which introduces additional phase shifts that are not accounted for in the standard geometrical equations describing radar interferometry. Spatially varying patterns of atmospheric water vapor changes the local index of refraction, which, in turn, introduces spatially varying phase shifts to the individual interferograms. Since the two (or more) interferograms are acquired at different times, the temporal change in water vapor introduces a signal that could be on the same order of magnitude as that expected from surface deformation, as discussed by Goldstein (87). Another limitation of the technique is temporal decorrelation. Changes in the surface properties may lead to complete decorrelation of the images and no detectable deformation signature (78).

Current research is only beginning to realize the full potential of radar interferometry. Even though some significant problems still have to be solved before this technique will become fully operational, the next few years will undoubtedly see an explosion in the interest and use of radar interferometry data.

NONIMAGING RADARS

Scatterometers

Scatterometers measure the surface backscattering cross section precisely in order to relate the measurement to the geophysical quantities such as the ocean wind speed and the soil moisture (88). Since spatial resolution is not a very important parameter, it is usually sacrificed for better accuracy in the backscattering cross-section measurement. Typical resolution of a scatterometer is several tens of kilometers. Since the backscattering cross section depends strongly on the surface roughness and the dielectric constant, scatterometer measurements are used to determine these surface properties. For example, since ocean surface roughness is related to the ocean wind speed, scatterometers can be used to measure the ocean wind speed indirectly. Over land, backscattering cross-section measurements can be used to estimate the surface moisture content on a global scale. However, since the scatterometer resolution size is on the order of several kilometers, the retrieved information is not as useful as the one derived from a high-resolution imaging radar.

As wind blows over the ocean surface, the first wave that is generated by the coupling between wind and the ocean surface is the 1.7 cm waves. As the wind continues to blow, energy is transferred to other parts of the surface spectrum and the surface wave starts to grow. Since the ocean surface has a large dielectric constant for the microwave spectrum, the backscattering is mainly related to the surface roughness. Therefore, it is reasonable to believe that the backscattering cross section is sensitive to the wind speed via surface roughness (89). Since the surface roughness scale at the size of the radar wavelength strongly influences the backscattering cross section, the scatterometer wavelength should be at the centimeter scale in order to derive the surface wind speed. Specifically, the surface roughness size (Λ) responsible for backscattering is related to the radar wavelength λ as

$$\Lambda = \frac{\lambda}{2 \sin\theta} \tag{52}$$

where θ is the incidence angle. This wavelength Λ is also known as the Bragg wavelength which represents a resonance scale in the scattering surface.

As discussed in the signal fading and speckle section, radar return measurements are contaminated by the speckle noise. In order to measure the backscattering cross section accurately, a large number of independent observations must be averaged (90). This can be done in the frequency domain or the time domain. In scatterometry, a commonly adopted parameter for the backscattering cross-section measurement accuracy is K_p, defined as

$$K_p = \frac{\sqrt{\mathrm{var}\{\sigma_{0\,\mathrm{meas}}\}}}{\sigma_0} \tag{53}$$

which is the normalized standard deviation of the measured backscattering cross section (91). To obtain an accurate measurement, K_p must be minimized.

Once the received power is measured, the backscattering cross section can be determined by using the radar equation. In this process, the noise power is also estimated and subtracted from the received power. Then, this backscattering cross section is related to the wind vector via a geophysical model function (92). In general, a model function can be written as

$$\sigma_0 = F(U,\, f,\, \theta,\, \alpha,\, p,\, \ldots) \tag{54}$$

where U is the wind speed, f is the radar frequency, θ is the incidence angle, α is the azimuth angle, and p denotes the radar signal polarization. Due to a lack of rigorous theoretical models, empirical models have been used for scatterometry applications. The precise form of the model function is still debated and is currently the subject of intense study. Figure 19 shows a schematic of the model functions. As an example of a model function, Wentz et al. (93,94) have used SEASAT data to derive a Ku-band geophysical model function known as SASS-2.

From a geophysical model function, one can observe that σ_0 is a function of the radar azimuth angle relative to the

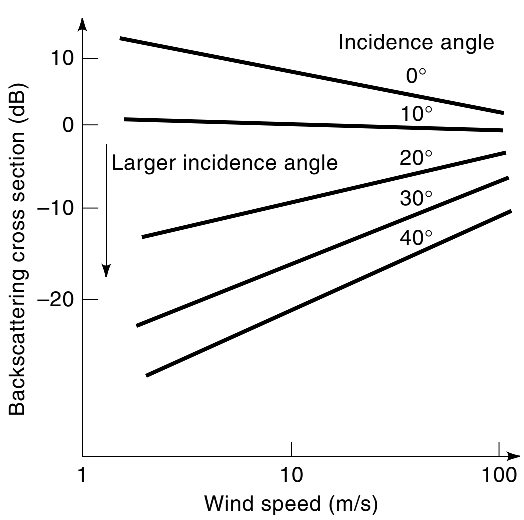

Figure 19. Schematic scatterometer model function. Using this geophysical model function, backscattering measurements are related to wind speed.

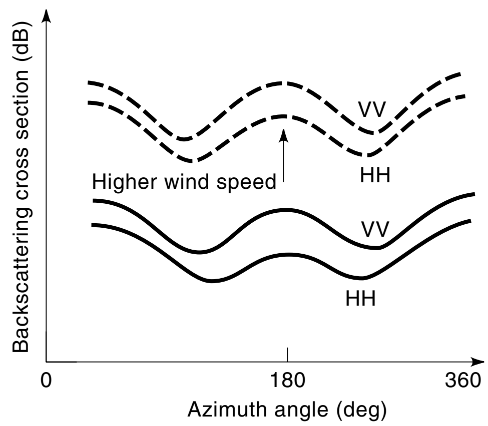

Figure 20. Backscattering cross section in terms of the radar azimuth angle relative to the wind direction. Note that σ_0 in the upwind direction is slightly higher than 1 in the downwind direction.

wind direction. Figure 20 shows the double sinusoidal relationship (92). That is, σ_0 is maximum at upwind ($\alpha = 0°$) and downwind ($\alpha = 180°$) directions, while it is minimum near the crosswind direction ($\alpha = 90°$ and $270°$). As can be seen from Fig. 20, σ_0 in the upwind direction is slightly higher than σ_0 in the downwind direction. In principle, a unique wind vector can be determined due to this small asymmetry. However, extremely accurate measurements are required to detect this small difference. It is clear that more than one σ_0 measurement must be made at different azimuth angles to determine the wind direction. In order to explain the wind direction determination technique, we use a simple model given by

$$\sigma_0 = AU^{\gamma}(1 + a\cos\alpha + b\cos 2\alpha) \tag{55}$$

where A, a, b, and γ are empirically determined for the wind speed U measured at a reference altitude (usually at 19.5 m above the ocean surface). As can be seen from Eq. (55), two measurements provide the wind speed U and the wind direction with a fourfold ambiguity; therefore, additional measurements are needed to remove the ambiguity. Otherwise, auxiliary meteorological information is required to select the correct wind direction from ambiguous vectors (95).

Spaceborne scatterometers are capable of measuring global wind vectors over oceans to be used to study upper ocean circulation, tropospheric dynamics, and air–sea interaction. Examples of spaceborne scatterometers are SASS (SEASAT scatterometer), ERS-1 (96,97), and NSCAT. Their radar parameters are shown in Table 1.

To estimate a wind vector, multiple colocated σ_0 measurements from different azimuth angles are required. Hence, the antenna subsystem is the most important component in the

Table 1. Spaceborne Scatterometer Parameters

	SASS	ERS-1	NSCAT
Frequency	14.6 GHz	5.3 GHz	14 GHz
Spatial resolution	50 km	50 km	25, 50 km
Swath width	500 km	500 km	600 km
Number of antennas	4	3	6
Polarization	VV, HH	VV	VV, HH
Orbit altitude	800 km	785 km	820 km

scatterometer design. Multiple fan beam and scanning spot beam antennas are widely used configurations. The next-generation scatterometer, known as SeaWinds, implements a scanning pencil-beam instrument in order to avoid the difficulties of accommodating a traditional fan-beam space scatterometer. The RF and digital subsystems of a scatterometer are similar to other radars except for a noise source for onboard calibration. Both internal and external calibration devices are required for a scatterometer to provide accurate backscattering cross-section measurements.

The resolution along the flight track can be improved by applying the Doppler filtering technique to the received echo. That is, if the echo is passed through a bandpass filter with a center frequency f_D and a bandwidth Δf, then the surface resolution Δx can be improved as

$$\Delta x = \frac{h\Delta f\left(\frac{2v}{\lambda}\right)^2}{\left[\left(\frac{2v}{\lambda}\right)^2 - f_D^2\right]^{3/2}} \tag{56}$$

where h is the platform altitude and v is the platform velocity (88).

Altimeters

A radar altimeter (88) measures the distance between the sensor and the surface at the nadir direction to derive a topographic map of the surface. Ranging accuracy of a spaceborne radar altimeter is a few tens of centimeters. Even though an altimeter can measure the land surface topography, the resulting topographic map is not very useful since the resolution of a radar altimeter is on the order of a few kilometers. However, this is satisfactory for oceanographic applications since high-resolution measurements are not required.

The geoid is the equipotential surface that corresponds to the mean sea level. Since the geoid is the static component of the ocean surface topography, it can be derived by averaging repetitive measurements over a long time period. The spatial variation in the geoid provides information on different geoscientific parameters. For example, large-scale variations (~1000 km) in the geoid are related to processes occurring deep in the Earth's interior.

A radar altimeter transmits a short pulse to the nadir direction and measures the round-trip time (T) accurately. Hence, the distance (H) from the sensor to the surface can be calculated from

$$H = \frac{vT}{2} \tag{57}$$

Here, v is the speed of a radar wave in the propagating medium. The height error (ΔH) can be written in terms of the velocity error (δv) and the timing error (δT) as

$$\delta H = \frac{T\delta v}{2} + \frac{v\delta T}{2} \tag{58}$$

The velocity error results from the refractive index variation due to ionosphere and atmosphere. The timing error is mainly related to the finite signal bandwidth and the clock accuracy on the spacecraft. In addition, small-scale roughness variation due to surface elevation causes an electromagnetic bias (98). This bias is about 1% of the significant wave height (SWH). These errors must be estimated and corrected to achieve the required height accuracy.

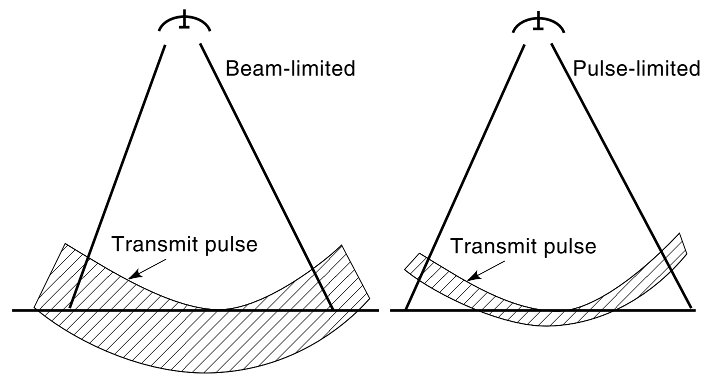

Figure 21. Beam-limited and pulse-limited altimeter footprints.

The altimeter resolution can be determined by either the radar beamwidth or the pulse length. If the beam footprint is smaller than the pulse footprint, the altimeter is called beam-limited. Otherwise, it is pulse-limited (see Fig. 21). The beam-limited footprint is given by $\lambda h/L$, while the pulse limited footprint is $2\sqrt{c\tau h}$, where h is the altitude, L is the antenna length, and τ is the pulse length.

The altimeter mean return waveform $W(t)$ (99,100) can be written as

$$W(t) = F(t)^* q(t)^* p(t) \tag{59}$$

where $F(t)$ is the flat surface impulse response including radar antenna beamwidth and pointing angle effects, $q(t)$ is the surface height probability density function, and $p(t)$ is the radar system impulse response. Here, the symbol * denotes the convolution operator. As illustrated in Fig. 22, the return pulse shape changes for different surface roughness.

As an example of radar altimeters, we briefly describe the TOPEX radar altimeter (101) that has been used to measure the sea level precisely. The resulting rms height accuracy of a single-pass measurement is 4.7 cm (102). This information is used to study the circulation of the world's oceans. The TOPEX altimeter is a dual-frequency (5.3 GHz and 13.6 GHz) radar in order to retrieve the ionospheric delay of the radar

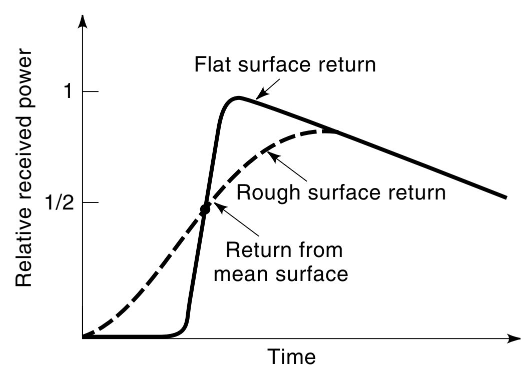

Figure 22. Altimeter return pulse shape for different surface roughnesses.

signal since ionosphere is a dispersive medium. The TOPEX microwave radiometer measures sea surface emissivity at three frequencies (18 GHz, 21 GHz, and 37 GHz) to estimate the total water vapor content. In addition, the satellite carries a global positioning system (GPS) receiver for precise satellite tracking. All these measurements are used to produce high-accuracy altimeter data. Recent research topics related to radar altimetry can be found in Ref. 102.

Radar Sounders

Radar sounders are used to image subsurface features by measuring reflections from dielectric constant variations. For example, an ice sounding radar can measure the ice thickness by detecting the ice–ocean boundary (103). In order to penetrate into subsurface, a long-wavelength radar is desired. Various radar sounding techniques are well-summarized in Ref. 104. In order to image subsurface features, a radar signal must penetrate to the target depth for satisfactory SNR. Like other radars, subsurface radar should have an adequate bandwidth for sufficient resolution to detect buried objects or other dielectric discontinuity.

For a ground penetrating radar (105), a probing antenna must be designed for efficient coupling of electromagnetic radiation into the ground. The depth resolution can be obtained by using similar techniques described in the previous sections. However, the physical distance must be estimated from the slant range information and the real part of the medium refractive index. In order to enhance horizontal resolution, one can use the synthetic aperture technique. However, the matched filter construction is very difficult since the medium dielectric constant is usually inhomogeneous and unknown. The most important quantity to design a subsurface radar is the medium loss that determines the penetration depth. For a ground subsurface radar, it is advantageous to average many samples or increase effective pulse length to enhance SNR. Polarimetric information is also important when buried objects are long and thin since strong backscattering is produced by a linearly polarized signal parallel to the long axis.

For an airborne (106) or a spaceborne radar sounder (107), subsurface returns must be separated from unwanted surface returns. Since a surface return is usually much stronger than a subsurface return, the radar must be designed for extremely low sidelobe. A surface return can be an ambiguous signal if it is at the same range as a subsurface return (surface ambiguity). This problem becomes more serious as the altitude of a radar becomes higher or the antenna gain becomes lower. Clearly, future research activities are required to overcome this difficulty. In addition, when the medium loss is large, the radar must have a large dynamic range to detect the small subsurface return.

As an example of orbiting radar sounders, we will briefly describe the Apollo 17 lunar sounder radar (107). The objectives of the sounder experiment were to detect subsurface geological structures and to generate a lunar surface profile. Since lunar soil and rock exhibit less attenuation due to the absence of free water, one may expect deeper subsurface penetration compared with the observations on Earth. This sounder, operating at three frequencies (5 MHz, 15 MHz, and 150 MHz), was also used to generate a lunar surface profile using the strong surface return.

Cloud Radar

Most meteorological radars (108) operate at centimeter wavelengths in order to avoid the significant attenuation by precipitation. However, cloud radars operate at millimeter wavelength since clouds cannot be observed easily by using conventional centimeter wavelength radars (109). In order to minimize absorption, the radar frequency must be in the spectral windows whose center frequencies are 35 Hz, 100 Hz, and 150 GHz. The first millimeter wave radar observations of clouds were done in the 35 GHz window (110). Benefiting from the technology development at 94 GHz, a 94 GHz spaceborne cloud radar has been proposed where even higher radar reflectivity is expected at a shorter wavelength. For a cloud radar, high dynamic range and low sidelobes are required to detect a weak signal scattered from a cloud in presence of large surface return.

For a pulsed radar, the received power (P_r) can be written as

$$P_r = \frac{P_t G^2 \lambda^2 V}{(4\pi)^3 r^4} \eta e^{-2\alpha} \tag{60}$$

where P_t is the peak transmit power, G is the antenna gain, λ is the wavelength, V is the resolution volume, η is the volumetric radar cross section, and α is the one-way loss (111). If the cloud particles are much smaller than the radar wavelength, using the Rayleigh scattering method, the radar reflectivity (Z) can be written as

$$Z = \frac{\eta \lambda^4}{\pi^5 |K|^2} \tag{61}$$

where $K = (n^2 - 1)/(n^2 + 2)$ and n is the complex refractive index of a particle. The radial velocity (v_r) is measured by using the Doppler frequency (f_d) as

$$v_r = \frac{f_d \lambda}{2} \tag{62}$$

Cloud radar measurements provide radar reflectivity and radial velocity profiles in terms of altitude. Recent airborne cloud radars (112,113) can measure polarimetric reflectivity which can provide the additional information such as the linear depolarization ratio (LDR). Using these parameters, a cloud region classification (ice, cloud droplets, mixed-phase hydrometeors, rain, and insects) can be achieved (111). If multiwavelength measurements are made, it may be possible to estimate the drop size distribution.

Rain Radar

The accurate measurement of rainfall is an important factor in understanding the global water and energy cycle. Rain radars measure the rain reflectivity that can be used to estimate the parameters related to rainfall using inversion algorithms (114). As an example of rain radars, one of tropical rainfall measuring mission (TRMM) (115) instruments is a single-frequency (13.8 GHz) , cross-track scanning radar for precipitation measurement. The satellite altitude is 350 km and the scanning swath is 220 km. The range and surface horizontal resolutions are 250 m and 4 km, respectively. Using TRMM data, rain profiles can be estimated (114).

The operation frequency (13.8 GHz) is selected by considering both antenna size and attenuation. At this frequency, the antenna size does not have to be too large and the attenuation is small enough to measure rainfall near the surface. As an airborne rain radar, the National Aeronautics and Space Administration and the Jet Propulsion Laboratory developed an airborne rain-mapping radar (ARMAR) that flies on the NASA DC-8 aircraft (116). ARMAR operates with TRMM frequency and geometry to understand the issues related to TRMM rain radar.

Due to the downward looking geometry, it is possible that surface clutter return may obscure the return from precipitation. Even for an antenna looking off-nadir, the nadir return can be at the same range as precipitation. In order to overcome these difficulties, both antenna sidelobes and pulse compression sidelobes must be low (~ -60 dB relative to the peak return) enough to detect precipitation. In order to measure rain reflectivity accurately, it is necessary to calibrate the radar precisely. Radar measurements such as the reflectivity, the H and V polarization phase difference, and the differential reflectivity (HH and VV) can be used to estimate rain rate and rain profile.

BIBLIOGRAPHY

1. C. Elachi, *Introduction to the Physics and Techniques of Remote Sensing,* New York: Wiley, 1987.
2. F. T. Ulaby, R. K. Moore, and A. K. Fung, Microwave remote sensing: active and passive, *Radar Remote Sensing and Surface Scattering and Emission Theory,* Vol. 2, Dedham, MA: Artech House, 1982.
3. J. C. Curlander and R. N. McDonough, *Synthetic Aperture Radar Systems and Signal Processing,* New York: Wiley, 1991.
4. J. P. Ford, Resolution versus speckle relative to geologic interpretability of spaceborne radar images: A survey of user preferences, *IEEE Trans. Geosci. Remote Sens.,* **GRS-20**: 434–444, 1982.
5. H. A. Zebker, J. J. van Zyl, and D. N. Held, Imaging radar polarimetry from wave synthesis, *J. Geophys. Res.,* **92**: 683–701, 1987.
6. R. L. Jordan, B. L. Huneycutt, and M. Werner, The SIR-C/X-SAR synthetic aperture radar system, *IEEE Trans. Geosci. Remote Sens.,* **GRS-33**: 829–839, 1995.
7. J. J. van Zyl, A technique to calibrate polarimetric radar images using only image parameters and trihedral corner reflectors, *IEEE Trans. Geosci. Remote Sens.,* **GRS-28**: 337–348, 1990.
8. H. A. Zebker and Y. L. Lou, Phase calibration of imaging radar polarimeter Stokes matrices, *IEEE Trans. Geosci. Remote Sens.,* **GRS-28**: 246–252, 1990.
9. A. L. Gray et al., Synthetic aperture radar calibration using reference reflectors, *IEEE Trans. Geosci. Remote Sens.,* **GRS-28**: 374–383, 1990.
10. A. Freeman, Y. Shen, and C. L. Werner, Polarimetric SAR calibration experiment using active radar calibrators, *IEEE Trans. Geosci. Remote Sens.,* **GRS-28**: 224–240, 1990.
11. J. D. Klein and A. Freeman, Quadpolarisation SAR calibration using target reciprocity, *J. Electromagn. Waves Appl.,* **5**: 735–751, 1991.
12. H. A. Zebker et al., Calibrated imaging radar polarimetry: Technique, examples, and applications, *IEEE Trans. Geosci. Remote Sens.,* **GRS-29**: 942–961, 1991.
13. A. Freeman et al., Calibration of Stokes and scattering matrix format polarimetric SAR data, *IEEE Trans. Geosci. Remote Sens.,* **GRS-30**: 531–539, 1992.
14. A. Freeman, SAR calibration: An overview, *IEEE Trans. Geosci. Remote Sens.,* **GRS-30**: 1107–1121, 1992.
15. A. Freeman et al., SIR-C data quality and calibration results, *IEEE Trans. Geosci. Remote Sens.,* **GRS-33**: 848–857, 1995.
16. J. A. Kong et al., Identification of earth terrain cover using the optimum polarimetric classifier, *J. Electromagn. Waves Appl.,* **2**: 171–194, 1988.
17. H. H. Lim et al., Classification of earth terrain using polarimetric synthetic aperture radar images, *J. Geophys. Res.,* **94**: 7049–7057, 1989.
18. J. J. van Zyl and C. F. Burnette, Bayesian classification of polarimetric sar images using adaptive *a priori* probabilities, *Int. J. Remote Sens.,* **13**: 835–840, 1992.
19. E. Rignot and R. Chellappa, Segmentation of polarimetric synthetic aperture radar data, *IEEE Trans. Image Process.,* **1**: 281–300, 1992.
20. E. Rignot and R. Chellappa, Maximum *a-posteriori* classification of multifrequency, multilook, synthetic aperture radar intensity data, *J. Opt. Soc. Amer. A,* **10**: 573–582, 1993.
21. E. J. M. Rignot et al., Mapping of forest types in Alaskan boreal forests using SAR imagery, *IEEE Trans. Geosci. Remote Sens.,* **GRS-32**: 1051–1059, 1994.
22. L. E. Pierce et al., Knowledge-based classification of polarimetric SAR images, *IEEE Trans. Geosci. Remote Sens.,* **GRS-32**: 1081–1086, 1994.
23. J. J. van Zyl, Unsupervised classification of scattering behavior using radar polarimetry data, *IEEE Trans. Geosci. Remote Sens.,* **GRS-27**: 36–45, 1989.
24. L. L. Hess et al., Delineation of inundated area and vegetation along the amazon floodplain with the SIR-C synthetic aperture radar, *IEEE Trans. Geosci. Remote Sens.,* **GRS-33**: 896–904, 1995.
25. R. H. Lang and J. S. Sidhu, Electromagnetic backscattering from a layer of vegetation, *IEEE Trans. Geosci. Remote Sens.,* **GRS-21**: 62–71, 1983.
26. J. A. Richards, G. Sun, and D. S. Simonett, L-Band radar backscatter modeling of forest stands, *IEEE Trans. Geosci. Remote Sens.,* **GRS-25**: 487–498, 1987.
27. S. L. Durden, J. J. van Zyl, and H. A. Zebker, Modeling and observation of the radar polarization signature of forested areas, *IEEE Trans. Geosci. Remote Sens.,* **GRS-27**: 290–301, 1989.
28. F. T. Ulaby et al., Michigan microwave canopy scattering model, *Int. J. Remote Sens.,* **11**: 1223–1253, 1990.
29. N. Chauhan and R. Lang, Radar modeling of a boreal forest, *IEEE Trans. Geosci. Remote Sens.,* **GRS-29**: 627–638, 1991.
30. G. Sun, D. S. Simonett, and A. H. Strahler, A radar backscatter model for discontinuous coniferous forest canopies, *IEEE Trans. Geosci. Remote Sens.,* **GRS-29**: 639–650, 1991.
31. S. H. Yueh et al., Branching model for vegetation, *IEEE Trans. Geosci. Remote Sens.,* **GRS-30**: 390–402, 1992.
32. Y. Wang, J. Day, and G. Sun, Santa Barbara microwave backscattering model for woodlands, *Int. J. Remote Sens.,* **14**: 1146–1154, 1993.
33. C. C. Hsu et al., Radiative transfer theory for polarimetric remote sensing of pine forest at P-Band, *Int. J. Remote Sens.,* **14**: 2943–2954, 1994.
34. R. H. Lang et al., Modeling P-Band SAR returns from a red pine stand, *Remote Sens. Environ.,* **47**: 132–141, 1994.
35. M. C. Dobson et al., Dependence of radar backscatter on conifer forest biomass, *IEEE Trans. Geosci. Remote Sens.,* **GRS-30**: 412–415, 1992.

36. T. LeToan et al., Relating forest biomass to SAR data, *IEEE Trans. Geosci. Remote Sens.,* **GRS-30**: 403–411, 1992.

37. K. J. Ranson and G. Sun, Mapping biomass of a northern forest using multifrequency SAR data, *IEEE Trans. Geosci. Remote Sens.,* **GRS-32**: 388–396, 1994.

38. A. Beaudoin et al., Retrieval of forest biomass from SAR data, *Int. J. Remote Sens.,* **15**: 2777–2796, 1994.

39. E. Rignot et al., Radar estimates of aboveground biomass in boreal forests of interior Alaska, *IEEE Trans. Geosci. Remote Sens.,* **GRS-32**: 1117–1124, 1994.

40. M. L. Imhoff, Radar backscatter and biomass saturation: Ramifications for global biomass inventory, *IEEE Trans. Geosci. Remote Sens.,* **GRS-33**: 511–518, 1995.

41. E. J. Rignot, R. Zimmerman, and J. J. van Zyl, Spaceborne applications of P-Band imaging radars for measuring forest biomass, *IEEE Trans. Geosci. Remote Sens.,* **GRS-33**: 1162–1169, 1995.

42. K. J. Ranson, S. Saatchi, and G. Sun, Boreal forest ecosystem characterization with SIR-C/XSAR, *IEEE Trans. Geosci. Remote Sens.,* **GRS-33**: 867–876, 1995.

43. M. C. Dobson et al., Estimation of forest biophysical characteristics in northern Michigan with SIR-C/X-SAR, *IEEE Trans. Geosci. Remote Sens.,* **GRS-33**: 877–895, 1995.

44. E. S. Kasischke, N. L. Christensen, and L. L. Bourgeau-Chavez, Correlating radar backscatter with components of biomass in loblolly pine forests, *IEEE Trans. Geosci. Remote Sens.,* **GRS-33**: 643–659, 1995.

45. Y. Oh, K. Sarabandi, and F. T. Ulaby, An empirical model and an inversion technique for radar scattering from bare soil surfaces, *IEEE Trans. Geosci. Remote Sens.,* **GRS-30**: 370–381, 1992.

46. P. C. Dubois, J. J. van Zyl, and T. Engman, Measuring soil moisture with imaging radars, *IEEE Trans. Geosci. Remote Sens.,* **GRS-33**: 915–926, 1995.

47. J. Shi and J. Dozier, Inferring snow wetness using C-Band data from SIR-C's polarimetric synthetic aperture radar, *IEEE Trans. Geosci. Remote Sens.,* **GRS-33**: 905–914, 1995.

48. L. C. Graham, Synthetic interferometer radar for topographic mapping, *Proc. IEEE,* **62**: 763–768, 1974.

49. H. Zebker and R. Goldstein, Topographic mapping from interferometric SAR observations, *J. Geophys. Res.,* **91**: 4993–4999, 1986.

50. H. A. Zebker et al., The TOPSAR interferometric radar topographic mapping instrument, *IEEE Trans. Geosci. Remote Sens.,* **GRS-30**: 933–940, 1992.

51. N. P. Faller and E. H. Meier, First results with the airborne single-pass DO-SAR interferometer, *IEEE Trans. Geosci. Remote Sens.,* **GRS-33**: 1230–1237, 1995.

52. J. E. Hilland et al., Future NASA spaceborne missions, *Proc. 16th Digital Avionics Syst. Conf.,* Irvine, CA, 1997.

53. S. N. Madsen, H. A. Zebker, and J. Martin, Topographic mapping using radar interferometry: Processing techniques, *IEEE Trans. Geosci. Remote Sens.,* **GRS-31**: 246–256, 1993.

54. R. M. Goldstein, H. A. Zebker, and C. Werner, Satellite radar interferometry: Two-dimensional phase unwrapping, *Radio Sci.,* **23**: 713–720, 1988.

55. F. K. Li and R. M. Goldstein, Studies of multibaseline spaceborne interferometric synthetic aperture radars, *IEEE Trans. Geosci. Remote Sens.,* **GRS-28**: 88–97, 1990.

56. C. Prati and F. Rocca, Limits to the resolution of elevation maps from stereo sar images, *Int. J. Remote Sens.,* **11**: 2215–2235, 1990.

57. C. Prati et al., Seismic migration for SAR focusing: Interferometrical applications, *IEEE Trans. Geosci. Remote Sens.,* **GRS-28**: 627–640, 1990.

58. H. A. Zebker and J. Villasenor, Decorrelation in interferometric radar echoes, *IEEE Trans. Geosci. Remote Sens.,* **GRS-30**: 950–959, 1992.

59. C. Prati and F. Rocca, Improving slant range resolution with multiple SAR surveys, *IEEE Trans. Aerosp. Electron. Syst.,* **29**: 135–144, 1993.

60. A. K. Gabriel and R. M. Goldstein, Crossed orbit interferometry: Theory and experimental results from SIR-B, *Int. J. Remote Sens.,* **9**: 857–872, 1988.

61. F. Gatelli et al., The wavenumber shift in SAR interferometry, *IEEE Trans. Geosci. Remote Sens.,* **GRS-32**: 855–865, 1994.

62. H. A. Zebker et al., Accuracy of topographic maps derived from ERS-1 interferometric radar, *IEEE Trans. Geosci. Remote Sens.,* **GRS-32**: 823–836, 1994.

63. E. R. Stofan et al., Overview of results of spaceborne imaging radar-C, X-band synthetic aperture radar (SIR-C/X-SAR), *IEEE Trans. Geosci. Remote Sens.,* **GRS-23**: 817–828, 1995.

64. J. Moreira et al., X-SAR interferometry: First results, *IEEE Trans. Geosci. Remote Sens.,* **GRS-33**: 950–956, 1995.

65. A. L. Gray and P. J. Farris-Manning, Repeat-pass interferometry with airborne synthetic aperture radar, *IEEE Trans. Geosci. Remote Sens.,* **GRS-31**: 180–191, 1993.

66. A. Moccia and S. Vetrella, A tethered interferometric synthetic aperture radar (SAR) for a topographic mission, *IEEE Trans. Geosci. Remote Sens.,* **GRS-31**: 103–109, 1992.

67. H. A. Zebker et al., Mapping the world's topography using radar interferometry: The TOPSAT mission, *Proc. IEEE,* **82**: 1774–1786, 1994.

68. R. M. Goldstein and H. A. Zebker, Interferometric radar measurements of ocean surface currents, *Nature,* **328**: 707–709, 1987.

69. R. M. Goldstein, T. P. Barnett, and H. A. Zebker, Remote sensing of ocean currents, *Science,* **246**: 1282–1285, 1989.

70. M. Marom et al., Remote sensing of ocean wave spectra by interferometric synthetic aperture radar, *Nature,* **345**: 793–795, 1990.

71. M. Marom, L. Shemer, and E. B. Thronton, Energy density directional spectra of nearshore wave field measured by interferometric synthetic aperture radar, *J. Geophys. Res.,* **96**: 22125–22134, 1991.

72. D. R. Thompson and J. R. Jensen, Synthetic aperture radar interferometry applied to ship-generated internal waves in the 1989 Loch Linnhe experiment, *J. Geophys. Res.,* **98**: 10259–10269, 1993.

73. R. E. Carande, Estimating ocean coherence time using dual-baseline interferometric synthetic aperture radar, *IEEE Trans. Geosci. Remote Sens.,* **GRS-32**: 846–854, 1994.

74. L. Shemer and M. Marom, Estimates of ocean coherence time by interferometric SAR, *Int. J. Remote Sens.,* **14**: 3021–3029, 1993.

75. A. K. Gabriel, R. M. Goldstein, and H. A. Zebker, Mapping small elevation changes over large areas: Differential radar interferometry, *J. Geophys. Res.,* **94**: 9183–9191, 1989.

76. D. Massonnet et al., The displacement field of the Landers earthquake mapped by radar interferometry, *Nature,* **364**: 138–142, 1993.

77. D. Massonnet et al., Radar interferometric mapping of deformation in the year after the Landers earthquake, *Nature,* **369**: 227–230, 1994.

78. H. A. Zebker et al., On the derivation of coseismic displacement fields using differential radar interferometry: The Landers earthquake, *J. Geophys. Res.,* **99**: 19617–19634, 1994.

79. G. Peltzer, K. Hudnut, and K. Feigl, Analysis of coseismic displacement gradients using radar interferometry: New insights into the Landers earthquake, *J. Geophys. Res.,* **99**: 21971–21981, 1994.
80. G. Peltzer and P. Rosen, Surface displacement of the 17 May 1993 Eureka Valley, California, earthquake observed by SAR interferometry, *Science,* **268**: 1333–1336, 1995.
81. D. Massonnet, P. Briole, and A. Arnaud, Deflation of Mount Etna monitored by spaceborne radar interferometry, *Nature,* **375**: 567–570, 1995.
82. D. Massonnet and K. Freigl, Satellite radar interferometric map of the coseismic deformation field of the $M + 6.1$ Eureka Valley, California earthquake of May 17, 1993, *Geophys. Res. Lett.,* **22**: 1541–1544, 1995.
83. R. M. Goldstein et al., Satellite radar interferometry for monitoring ice sheet motion: Application to an Antarctic ice stream, *Science,* **262**: 1525–1530,1993.
84. I. R. Joughin, Estimation of ice-sheet topography and motion using interferometric synthetic aperture radar, Ph.D. thesis, Univ. of Washington, Seattle, 1995.
85. E. Rignot, K. Jezek, and H. G. Sohn, Ice flow dynamics of the Greenlandice sheet from SAR interferometry, *Geophys. Res. Lett.,* **22**: 575–578, 1995.
86. I. R. Joughin, D. P. Winebrenner, and M. A. Fahnestock, Observations of ice-sheet motion in Greenland using satellite radar interferometry, *Geophys. Res. Lett.,* **22**: 571–574, 1995.
87. R. M. Goldstein, Atmospheric limitations to repeat-track radar interferometry, *Geophys. Res. Lett.,* **22**: 2517–1520, 1995.
88. C. Elachi, *Spaceborne Radar Remote Sensing: Applications and Techniques,* New York: IEEE Press, 1988.
89. M. A. Donelan and W. J. Pierson, Radar scattering and equilibrium ranges in wind-generated waves with application to scatterometry, *J. Geophys. Res.,* **92**: 4971–5029, 1987.
90. W. J. Plant, The variance of the normalized radar cross section of the sea, *J. Geophys. Res.,* **96**: 20643–20654, 1991.
91. C. Y. Chi and F. K. Li, A comparative study of several wind estimation algorithms for spaceborne scatterometers, *IEEE Trans. Geosci. Remote Sens.,* **26**: 115–121, 1988.
92. F. M. Naderi, M. H. Freilich, and D. G. Long, Spaceborne radar measurement of wind velocity over the ocean—an overview of the NSCAT scatterometer system, *Proc. IEEE,* **79**: 850–866, 1991.
93. F. J. Wentz, S. Peteherych, and L. A. Thomas, A model function for ocean radar cross sections at 14.6 GHz, *J. Geophys. Res.,* **89**: 3689–3704, 1984.
94. F. J. Wentz, L. A. Mattox, and S. Peteherych, New algorithms for microwave measurements of ocean winds: Applications to SEASAT and the special sensor microwave imager, *J. Geophys. Res.,* **91**: 2289–2307, 1986.
95. M. G. Wurtele et al., Wind direction alies removal studies of SEASAT scatterometer-derived wind fields, *J. Geophys. Res.,* **87**: 3365–3377, 1982.
96. C. L. Rufenach, J. J. Bates, and S. Tosini, ERS-1 scatterometer measurements—Part I: The relationsihp between radar cross section and buoy wind in two oceanic regions, *IEEE Trans. Geosci. Remote Sens.,* **36**: 603–622, 1998.
97. C. L. Rufenach, ERS-1 scatterometer measurements—Part I: An algorithm for ocean-surface wind retrieval including light winds, *IEEE Trans. Geosci. Remote Sens.,* **36**: 623–635, 1998.
98. E. Rodriguez, Altimetry for non-Gaussian oceans: Height biases and estimation of parameters, *J. Geophys. Res.,* **93**: 14107–14120, 1988.
99. G. S. Brown, The average impulse response of a rough surface and its applications, *IEEE Trans. Antennas Propag.,* **AP-25**: 67–74, 1977.
100. D. B. Chelton, E. J. Walsh, and J. L. MacArthur, Pulse compression and sea level tracking in satellite altimetry, *J. Atmos. Oceanic Technol.,* **6**: 407–438, 1989.
101. A. R. Zieger et al., NASA radar altimeter for the TOPEX/POSEIDON project, *Proc. IEEE,* **79**: 810–826, 1991.
102. TOPEX/POSEIDON: Geophysical evaluation, *J. Geophys. Res.,* **99**: 1994.
103. R. Bindschadler et al., Surface velocity and mass balance of ice streams D and E, West Antarctica, *J. Glaciol.,* **42**: 461–475, 1996.
104. D. J. Daniels, D. J. Gunton, and H. F. Scott, Introduction to subsurface radar, *IEE Proc., Part F,* **135**: 278–320, 1988.
105. Special issue on ground penetrating radar, *J. Appl. Geophys.,* **33**: 1995.
106. T. S. Chuah, Design and development of a coherent radar depth sounder for measurement of Greenland ice sheet thickness, Radar Systems and Remote Sensing Laboratory RSL Technical Report 10470-5, Univ. of Kansas Center for Res., 1997.
107. L. J. Porcello et al., The Apollo lunar sounder radar system, *Proc. IEEE,* **62**: 769–783, 1974.
108. R. J. Doviak and D. S. Zrnic, *Doppler Radar and Weather Observations,* Orlando, FL: Academic Press, 1984.
109. R. M. Lhermitte, Cloud and precipitation remote sensing at 94 GHz, *IEEE Trans. Geosci. Remote Sens.,* **26**: 256–270, 1997.
110. P. V. Hobbs et al., Evaluation of a 35 GHz radar for cloud physics research, *J. Atmos. Oceanic Technol.,* **2**: 35–48, 1985.
111. S. P. Lohmeier et al., Classification of particles in stratiform clouds using the 33 and 95 Ghz polarimetric cloud profiling radar system (CPRS), *IEEE Trans. Geosci. Remote Sens.,* **35**: 256–270, 1997.
112. A. L. Pazmany et al., An airborne 95 GHz dual polarized radar for cloud studies, *IEEE Trans. Geosci. Remote Sens.,* **32**: 731–739, 1994.
113. G. A. Sadowy et al., The NASA DC-8 airborne cloud radar: Design and preliminary results, *Proc. IGARSS '97,* 1997, pp. 1466–1469.
114. Z. S. Haddad et al., The TRMM 'day-1' radar/radiometer combined rain-profiling algorithm, *J. Meteorol. Soc. Jpn.,* **75**: 799—809, 1997.
115. J. Simpson, R. F. Adler, and G. R. North, A proposed tropical rainfall measuring mission (TRMM) satellite, *Bull. Amer. Meteorol. Soc.,* **69**: 278—295, 1988.
116. S. L. Druden et al., ARMAR: An airborne rain-mapping radar, *J. Atmos. Oceanic Technol.,* **11**: 727—737, 1994.

JAKOB J. VAN ZYL
YUNJIN KIM
California Institute of Technology